Title

The adaptive immune system restrains Alzheimer's disease pathogenesis by modulating microglial function

Journal

Proceedings of the National Academy of Sciences of the United States of America, 113(9)

ISSN

0027-8424

Authors

Marsh, Samuel E
Abud, Edsel M
Lakatos, Anita
et al.

Publication Date

2016-03-01

DOI

10.1073/pnas.1525466113

Peer reviewed

The adaptive immune system restrains Alzheimer's disease pathogenesis by modulating microglial function

Samuel E. Marsh[a,b], Edsel M. Abud[a,b,1], Anita Lakatos[c,1], Alborz Karimzadeh[b,d], Stephen T. Yeung[c,2], Hayk Davtyan[e], Gianna M. Fote[a,b], Lydia Lau[c], Jason G. Weinger[d,3], Thomas E. Lane[b,c,d,4], Matthew A. Inlay[b,d], Wayne W. Poon[c], and Mathew Blurton-Jones[a,b,c,5]

[a]Department of Neurobiology and Behavior, University of California, Irvine, CA 92697; [b]Sue and Bill Gross Stem Cell Research Center, University of California, Irvine, CA 92697; [c]Institute for Memory Impairments and Neurological Disorders, University of California, Irvine, CA 92697; [d]Department of Molecular Biology and Biochemistry, University of California, Irvine, CA 92697; and [e]Department of Molecular Immunology, Institute for Molecular Medicine, Huntington Beach, CA 92647

Edited by Bruce S. McEwen, The Rockefeller University, New York, NY, and approved January 19, 2016 (received for review December 24, 2015)

The innate immune system is strongly implicated in the pathogenesis of Alzheimer's disease (AD). In contrast, the role of adaptive immunity in AD remains largely unknown. However, numerous clinical trials are testing vaccination strategies for AD, suggesting that T and B cells play a pivotal role in this disease. To test the hypothesis that adaptive immunity influences AD pathogenesis, we generated an immune-deficient AD mouse model that lacks T, B, and natural killer (NK) cells. The resulting "Rag-5xfAD" mice exhibit a greater than twofold increase in β-amyloid (Aβ) pathology. Gene expression analysis of the brain implicates altered innate and adaptive immune pathways, including changes in cytokine/chemokine signaling and decreased Ig-mediated processes. Neuroinflammation is also greatly exacerbated in Rag-5xfAD mice as indicated by a shift in microglial phenotype, increased cytokine production, and reduced phagocytic capacity. In contrast, immune-intact 5xfAD mice exhibit elevated levels of nonamyloid reactive IgGs in association with microglia, and treatment of Rag-5xfAD mice or microglial cells with preimmune IgG enhances Aβ clearance. Last, we performed bone marrow transplantation studies in Rag-5xfAD mice, revealing that replacement of these missing adaptive immune populations can dramatically reduce AD pathology. Taken together, these data strongly suggest that adaptive immune cell populations play an important role in restraining AD pathology. In contrast, depletion of B cells and their appropriate activation by T cells leads to a loss of adaptive–innate immunity cross talk and accelerated disease progression.

Alzheimer's | amyloid | inflammation | microglia | IgG

Alzheimer's disease (AD) is the leading cause of age-related neurodegeneration, affecting over 5.2 million people in the United States alone (1). Pathologically, AD is characterized by two hallmark protein aggregates, amyloid-β (Aβ) plaques and neurofibrillary tangles, that are accompanied by neuroinflammation, including microgliosis, elevated cytokine production, and activation of complement pathways (2–5). Initially, microglia respond to and surround plaques, degrading Aβ by phagocytosis (for review, see refs. 6–8). However, chronic activation of these cells shift microglia to a more proinflammatory and less phagocytic state (9, 10). Although much of the data implicating microglia in AD has come from neuropathological investigation, recent genome-wide association studies have provided the first genetic evidence (to our knowledge) linking microglia dysfunction to AD, with the discovery of risk polymorphisms in several immune system genes: CR1, TREM2, CD33, HLA-DRB5, MS4A6A, and ABCA7 (8, 11–15).

In contrast to the field's increasing understanding of the role of innate immunity in AD, comparatively little is known about whether the adaptive immune system might also influence AD. Those studies that have examined these peripheral populations have largely focused on questions about their potential as biomarkers or their role in active Aβ immunization (3, 16). However, the adaptive and innate immune systems rarely function independently of each other, and thus cross talk between peripheral and central immunity such as cytokine and chemokine signaling likely plays an important albeit understudied role in AD. In support of this notion, two recent studies demonstrated profound effects of peripherally derived neutrophils and T-regulatory cells (Tregs) on AD pathogenesis (17, 18). Despite this exciting recent progress, many of the mechanisms and actions of other peripheral immune cell populations in AD remain unknown, and thus a great a deal of additional study is needed.

Here, we show that the adaptive immune system plays an important role in limiting amyloid pathology in AD, by generating and examining a novel immune-deficient transgenic model of AD. The resulting "Rag-5xfAD" mice, which lack an adaptive immune response, exhibit dramatically increased Aβ plaque load, despite already being a very aggressive model of amyloidosis. Gene ontology (GO) analysis revealed significant alterations in cytokine/chemokine signaling and microglial associated pathways that were validated at the protein level. Furthermore, peripherally derived nonamyloid reactive immunoglobulin G (IgG) appears to enter the brain and enhance microglial phagocytosis of Aβ in immune-intact mice,

Significance

Neuroinflammation and activation of innate immunity are pathological hallmarks of Alzheimer's disease (AD). In contrast, very few studies have examined the impact of the adaptive immune system in AD pathogenesis. Here, we find that genetic ablation of peripheral immune cell populations significantly accelerates amyloid pathogenesis, worsens neuroinflammation, and alters microglial activation state. Critically, it appears that loss of IgG-producing B cells impairs microglial phagocytosis, thereby exacerbating amyloid deposition. Conversely, replacement of IgGs via direct injection or bone marrow transplantation reverses these effects and reduces Aβ pathology. Together, these results highlight the importance of the adaptive immune system and its interactions with microglia in the pathogenesis of AD.

Author contributions: S.E.M., E.M.A., A.L., A.K., H.D., J.G.W., T.E.L., M.A.I., W.W.P., and M.B.-J. designed research; S.E.M., E.M.A., A.L., A.K., S.T.Y., H.D., G.M.F., L.L., J.G.W., W.W.P., and M.B.-J. performed research; S.E.M., E.M.A., A.L., A.K., S.T.Y., H.D., G.M.F., J.G.W., T.E.L., M.A.I., W.W.P., and M.B.-J. analyzed data; and S.E.M., E.M.A., W.W.P., and M.B.-J. wrote the paper.

The authors declare no conflict of interest.

This article is a PNAS Direct Submission.

Freely available online through the PNAS open access option.

Data deposition: The data reported in this paper have been deposited in the Gene Expression Omnibus (GEO) database, www.ncbi.nlm.nih.gov/geo (accession no. GSE77574).

[1]E.M.A. and A.L. contributed equally to this work.

[2]Present address: Department of Immunology, University of Connecticut School of Medicine, Farmington, CT 06030.

[3]Present address: Neurocentria, Inc., Fremont, CA 94538.

[4]Present address: Department of Pathology, University of Utah School of Medicine, Salt Lake City, UT 84112.

[5]To whom correspondence should be addressed. Email: mblurton@uci.edu.

This article contains supporting information online at www.pnas.org/lookup/suppl/doi:10.1073/pnas.1525466113/-/DCSupplemental.

whereas the loss of this protective mechanism in immune-deficient Rag-5xfAD mice appears to accelerate AD progression. Conversely, replacement of IgGs by either direct injection or bone marrow transplantation reduces Aβ pathology in Rag-5xfAD mice. Taken together, these studies suggest that alterations in peripheral immune function such as those that occur with age, comorbid diseases, or genetic variation could dramatically affect the development and progression of AD.

Results

Generation of an Immune-Deficient AD Mouse Model. To examine the impact of the adaptive immune system on AD pathogenesis, we backcrossed a well-established AD transgenic line, 5xfAD mice (19), onto a Rag2$^{-/-}$/Il2rγ$^{-/-}$ double-knockout background, creating mice that lacked T cells, B cells, and natural killer (NK) cells. Although NK cells are typically considered part of the innate immune system, recent studies suggest they also play important roles in adaptive immunity (20). In the process of generating these immune-deficient Rag-5xfAD and "Rag-WT" littermates, we also produced strain-matched equivalent immune-competent AD transgenic and wild-type mice termed "WT-5xfAD" and "WT-WT," respectively (Fig. S1). Although the parental 5xfAD mice are maintained on a purebred C57Bl6 strain, the Rag2$^{-/-}$/Il2rγ$^{-/-}$ line is maintained as a C57Bl6/Bl10 hybrid. To verify that the resulting lines exhibited equivalent genetic backgrounds, we therefore examined tail DNA using a 384 mouse SNP array (Charles River Laboratories), which revealed equivalent mixtures of Bl6 and Bl10 alleles in each group.

To confirm that the resulting Rag-5xfAD and Rag-WT mice lacked B, T, and NK cells, flow cytometry was performed on splenocytes extracted from 6-mo-old mice. Analysis confirmed that all immune-deficient animals, regardless of AD transgene expression, lacked B cells, CD4 and CD8 T cells, as well as NK cells and NK T cells (Fig. S1 *B–E*). Given the large role of inflammation in the pathogenesis of AD, we also examined whether immune-competent animals exhibited altered proportions of these immune cells. Analysis of splenocytes by flow cytometry found that percentages of B, CD8 T, NK, and NK-T cells were all unchanged with 5xfAD transgene expression. However, there was a small but significant difference in the percentages of CD4 T cells between the WT-WT and WT-5xfAD animals (Fig. S1 *B–E*).

Aβ Levels Are Dramatically Increased in Rag-5xfAD Mice. To determine whether deletion of these peripheral immune cell populations influences AD pathogenesis, we performed a highly sensitive multiplex ELISA to quantify soluble and insoluble levels of Aβ within the brain. Surprisingly, and despite the use of an aggressive model of amyloidosis, we found that all Aβ species examined (Aβ38, 40, 42) were elevated nearly twofold in Rag-5xfAD vs. WT-5xfAD half-brains (Fig. 1 *A* and *B*). Additionally, immunohistochemistry was performed and plaque volume calculated from confocal *z*-stack images using IMARIS image analysis software (Fig. 1 *C* and *D*). Analysis of the dentate gyrus of the hippocampus, one of the most plaque-dense areas in the 5xfAD model, revealed that Rag-5xfAD mice exhibited a highly significant ($P < 0.001$), nearly fourfold increase in total plaque volume in this region (Fig. 1*E*). Quantification of small-, medium-, and large-sized plaques also revealed that Rag-5xfAD animals exhibit 2.5- to 3-fold increases in the number of plaques of each size compared with WT-5xfAD ($P < 0.05$; Fig. 1*F*).

Increased Aβ Load Is Not a Result of Increased APP Expression or Aβ Production. Given the substantial increase in Aβ observed in Rag-5xfAD mice, we next sought to determine whether these findings arose from increased Aβ production or decreased clearance. Although autosomal-dominant AD is characterized primarily by mutations that increase production of Aβ or Aβ42/40 ratio (21, 22), recent studies demonstrate that sporadic AD patients primarily accumulate Aβ as a result of impaired clearance (23–25).

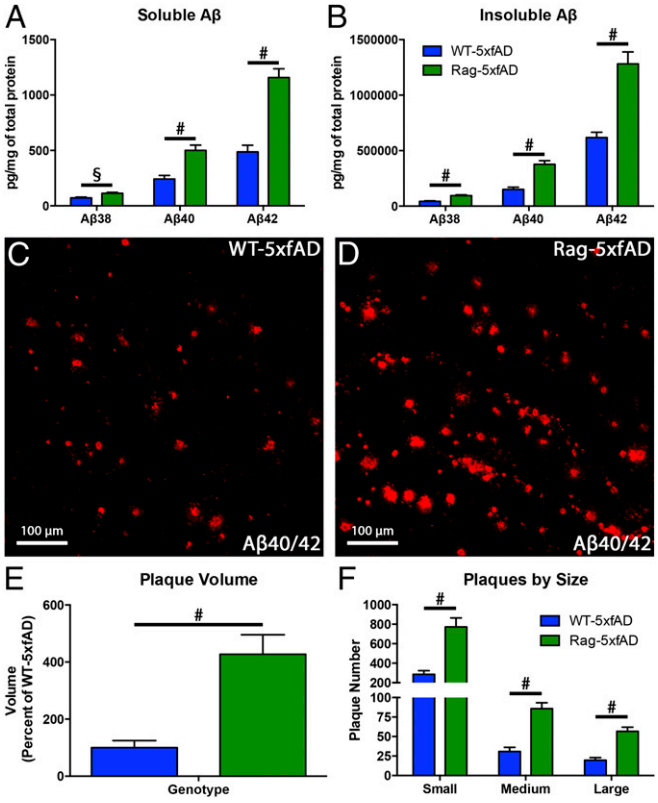

Fig. 1. Aβ is significantly elevated in immune-incompetent Rag-5xfAD mice. (*A* and *B*) Aβ multiplex ELISA reveals significant elevations in all three Aβ species in both soluble and insoluble brain lysates from Rag-5xfAD vs. WT-5xfAD. Representative confocal images of Aβ40/42-immunoreactive plaques within the dentate gyrus demonstrates a similar robust change in plaque load between WT-5xfAD (*C*) and Rag-5xfAD mice (*D*). (*E*) IMARIS-based 3D quantification of Aβ confirms ELISA and immunohistochemical (IHC) findings, demonstrating a more than fourfold increase in dentate gyrus plaque volume in Rag-5xfAD mice (green) vs. WT-5xfAD mice (blue). (*F*) Stratification of dentate plaque numbers by size likewise reveals significant elevations in Rag-5xfAD mice. Data are represented as mean ± SEM. ANOVA, $P < 0.05$, and Fisher's protected least-significant difference (PLSD) post hoc, $^{§}P < 0.01$, $^{\#}P < 0.001$; $n \geq 8$ mice/group.

However, the 5xfAD model, as with most AD transgenic animals, includes familial AD mutations, and thus increased Aβ production could potentially underlie the observed changes in amyloid load. We therefore examined the protein levels of human amyloid precursor protein (APP) and Presenilin-1 (PS-1) by Western blot. Although Rag-5xfAD and WT-5xfAD mice exhibited the expected transgene-mediated increases in APP and PS-1 vs. wild-type controls, no differences in APP and PS-1 expression were detected between Rag-5xfAD and WT-5xfAD groups (Fig. S2 *A–C*). Furthermore, quantitative PCR (qPCR) analysis of APP processing genes found no significant changes in expression of h*APP*, h*PSEN1*, *Adam10*, *Adam17*, *Bace1*, and *Bace2* between WT-5xfAD and Rag-5xfAD (Fig. S2*D*). Thus, it appears that the observed elevations in plaque load in Rag-5xfAD are not due to increased APP production and/or processing, but rather likely mediated via altered Aβ clearance.

GO Analysis Implicates Disrupted Cross Talk Between Adaptive and Innate Immunity. Next, we used microarrays and functional genomic analysis to provide an unbiased assessment of the pathways that are altered in immune-deficient vs. immune-intact AD and wild-type mice. Whole-brain mRNA from all four groups was compared using Affymetrix Mouse Transcriptome 1.0 array, revealing 2,552 significantly altered genes between Rag-5xfAD and WT-5xfAD groups

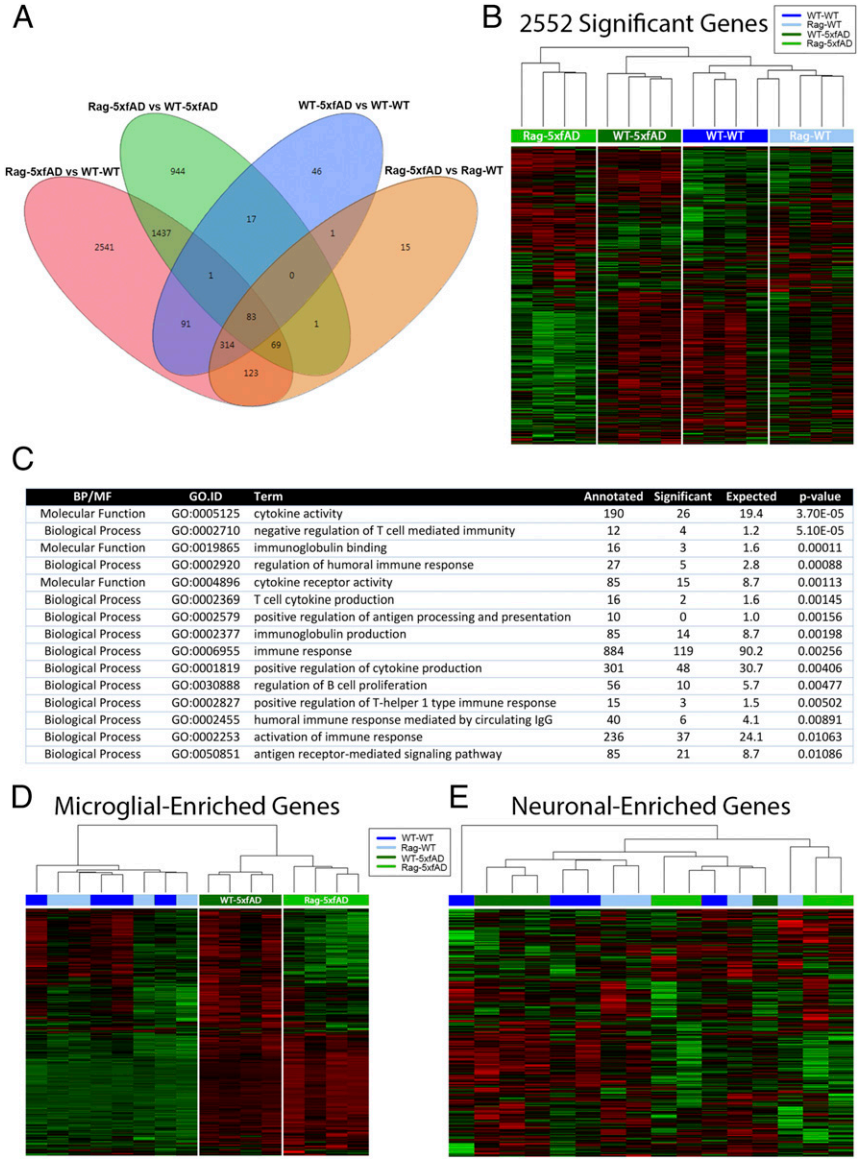

C

BP/MF	GO.ID	Term	Annotated	Significant	Expected	p-value
Molecular Function	GO:0005125	cytokine activity	190	26	19.4	3.70E-05
Biological Process	GO:0002710	negative regulation of T cell mediated immunity	12	4	1.2	5.10E-05
Molecular Function	GO:0019865	immunoglobulin binding	16	3	1.6	0.00011
Biological Process	GO:0002920	regulation of humoral immune response	27	5	2.8	0.00088
Molecular Function	GO:0004896	cytokine receptor activity	85	15	8.7	0.00113
Biological Process	GO:0002369	T cell cytokine production	16	2	1.6	0.00145
Biological Process	GO:0002579	positive regulation of antigen processing and presentation	10	0	1.0	0.00156
Biological Process	GO:0002377	immunoglobulin production	85	14	8.7	0.00198
Biological Process	GO:0006955	immune response	884	119	90.2	0.00256
Biological Process	GO:0001819	positive regulation of cytokine production	301	48	30.7	0.00406
Biological Process	GO:0030888	regulation of B cell proliferation	56	10	5.7	0.00477
Biological Process	GO:0002827	positive regulation of T-helper 1 type immune response	15	3	1.5	0.00502
Biological Process	GO:0002455	humoral immune response mediated by circulating IgG	40	6	4.1	0.00891
Biological Process	GO:0002253	activation of immune response	236	37	24.1	0.01063
Biological Process	GO:0050851	antigen receptor-mediated signaling pathway	85	21	8.7	0.01086

Fig. 2. Gene expression and ontology analysis reveal significant alterations in both adaptive and innate immunity and microglial-enriched genes. (*A*) Affymetrix gene expression analysis revealed 2,552 significantly altered genes between Rag-5xfAD (light green) and WT-5xfAD (dark green) groups. In contrast, only 553 genes were different between WT-5xfAD and WT-WT (dark blue) groups. Thus, the combination of AD transgenes and immune deficiency leads to a profound alteration in gene expression within the brain, well beyond that produced by AD pathology alone. (*B*) Hierarchical cluster analysis of these 2,552 differentially expressed genes confirmed that each genotype could be grouped together based on similar gene expression profiles (red, up-regulated; green, down-regulated). (*C*) Next, gene ontology (GO) enrichment was performed, identifying numerous examples of significantly altered pathways involving adaptive or innate immunity as well as antigen presentation and Ig binding. (*D* and *E*) Based on the GO analysis, we further examined subsets of microglial-enriched (*D*) or neuronal-enriched (*E*) genes (26) via unsupervised hierarchical clustering. This analysis again further implicated innate immune system disruption as the Rag-5xfAD and WT-5xfAD groups clustered very well via microglial-specific genes, but not via neuronal genes. In contrast, WT-WT (dark blue) and Rag-WT (light blue) groups did not cluster well together for either microglial or neuronal transcripts. $P < 0.05$ was defined as the cutoff to identify the statistical significance of enrichment analyses in *C*.

(Fig. 2 *A* and *B*). Interestingly, the great majority of these changes reflected decreased expression (green) of many T-cell– and B-cell–associated transcripts in Rag-5xfAD vs. WT-5xfAD mice (Fig. 2*B*), supporting the notion that these peripheral populations can be found within the brain. In contrast, many of the up-regulated genes (red) in Rag-5xfAD mice consisted of chemokine and cytokine signaling factors involved in recruitment of peripheral cells as well as altered microglial-enriched transcripts. Next, GO analysis was used to identify potential biological or signaling mechanisms that were significantly altered between Rag-5xfAD and WT-5xfAD brains. This analysis further implicated both adaptive and innate immunity as changes in GO terms such as cytokine activity, Ig binding, and antigen-receptor–mediated signaling were highly significant (Fig.2*C*). To determine whether changes affected microglia function and whether microglial-associated transcripts were specifically altered, we also performed hierarchical cluster analysis of microglial-enriched genes and compared these results to neuronally enriched mRNAs (Fig. 2 *D* and *E*), as identified from a recently published online RNA-seq database (26). As shown, Rag-5xfAD microglial gene expression clusters very well together but completely separate from WT-5xfAD mice. In addition, Rag-5xfAD mice exhibit profound increases (red) in the great majority of microglial transcripts

(Fig. 2*D*), far beyond that observed in WT-5xfAD mice compared with the WT-WT group. Interestingly, no significant changes are detected between WT-WT and Rag-WT microglial genes (Dataset S1) and these groups fail to separate by hierarchical clustering (Fig. 2*D*), suggesting that the impact of the adaptive immune system on microglial gene expression occurs primarily in response to AD pathology rather than an inherent developmental difference. In contrast to the interactions between AD pathology and immune deficiency on microglia gene expression, neuronal genes showed far greater variability as Rag5xfAD and WT-5xfAD groups failed to cluster together (Fig. 2*E*). Thus, changes in neuronal expression are far more variable and less systemic than the observed microglial alterations. Together, these analyses prompted us to further examine the role of microglia dysfunction in Rag-induced exacerbation of AD pathology.

Microglial Activation and Phagocytosis Is Altered in Rag-5xfAD Animals. Given that our genomic analysis strongly implicated microglial dysfunction, we next sought to determine whether alterations in microglial number or morphology could explain the increased Aβ. To quantify microglial number and to model the branching of microglial processes, immunohistochemical and IMARIS-based 3D analysis of Iba1+ microglia was performed (Fig. 3 *A–D*). Upon activation by reactive stimuli, microglial typically become more amoeboid with shorter and less complex processes that can be accurately quantified via unbiased IMARIS 3D rendering (7). Confocal *Z* stacks were captured from the dentate gyrus by a blinded observer, and then microglial number, process length, and branching were assessed. As expected, we found that WT-5xfAD mice exhibited substantial increases in microglial cell number vs. WT-WT mice and a corresponding reduction in microglial branching and process length, indicative of activated phenotype (Fig. 3 *E–G*). However, we also found that Rag-5xfAD mice exhibited an additional significant increase in microglial number and decreases in branching and process length vs. WT-5xfAD mice, suggesting that Rag-5xfAD microglia may be further or differentially activated relative to WT-5xfAD mice (Fig. 3 *E–G*). Interestingly, we also found that Rag-WT microglia had on average slightly longer processes and a small increase in branching vs. WT-WT microglia (Fig. 3 *F* and *G*). Thus, it appears that the loss of B, T, and NK cells can subtly modulate the phenotype of microglia within the brain in the absence of pathology.

Given the observed changes in microglial number and morphology in Rag-5xfAD mice, we reasoned that other alterations in microglial function likely occur. We therefore used a multiplex ELISA-based assay [Meso Scale Discovery (MSD) proinflammatory panel 1] to measured protein levels of several important cytokines within the brain. For each of these cytokines, we found no differences between WT-WT and Rag-WT mice (Fig. 3 *H–L*). In contrast, several key proinflammatory cytokines produced by microglia including interleukin 1β (IL-1β), interleukin 6 (IL-6), and tumor necrosis factor α (TNFα) were significantly elevated in WT-5xfAD animals compared with WT-WT mice. Furthermore, these same cytokines were even further elevated as much as twofold in Rag-5xfAD mice compared with WT-5xfAD (Fig. 3 *H–J*). Although levels of interferon-gamma (IFNγ) were significantly

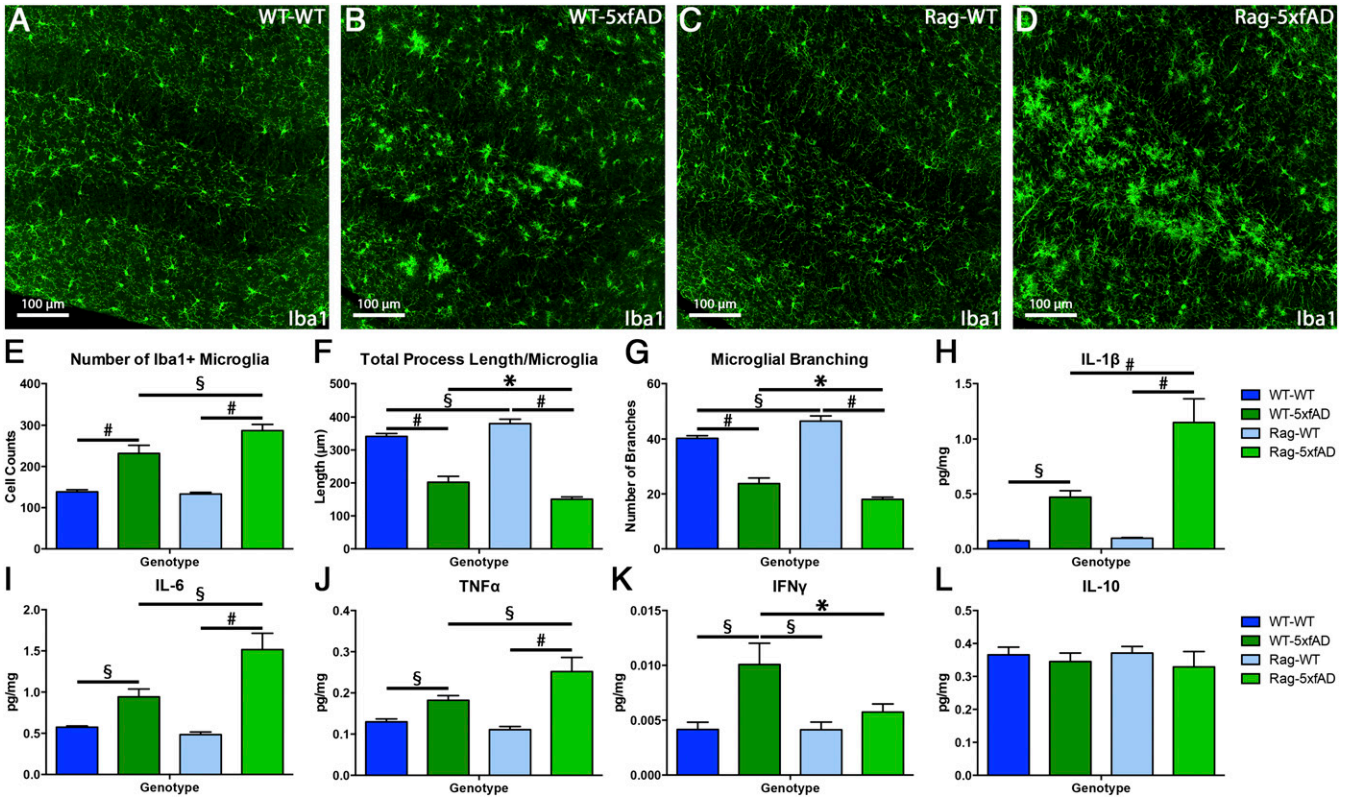

Fig. 3. Microglia morphology and brain cytokine profile are significantly altered in Rag-5xfAD mice. (*A–D*) Representative images of microglia (Iba1+) in the dentate gyrus of WT-WT, WT-5xfAD, Rag-WT, and Rag-5xfAD mice. (*E–G*) Automated analysis using IMARIS software illustrates that microglial number, total process length/microglia, and number of process branches/microglia are significantly altered by lack of adaptive immune system and AD pathology. (*H–J*) Results from MSD proinflammatory multiplex array reveal that Rag-5xfAD mice exhibit significant elevations in proinflammatory cytokines IL-1β, IL-6, and TNFα within the brain vs. WT-5xfAD mice. (*K*) However, IFNγ levels are unchanged from basal WT levels in Rag-5xfAD mice due to lack of IFNγ-producing T cells. (*L*) Levels of the antiinflammatory cytokine IL-10 are unchanged regardless of immune or transgene status. Data are represented as mean ± SEM. ANOVA, $P < 0.05$, and Fisher's PLSD post hoc, $^{*}P < 0.05$, $^{\S}P < 0.01$, $^{\#}P < 0.001$; $n \geq 8$ animals/group.

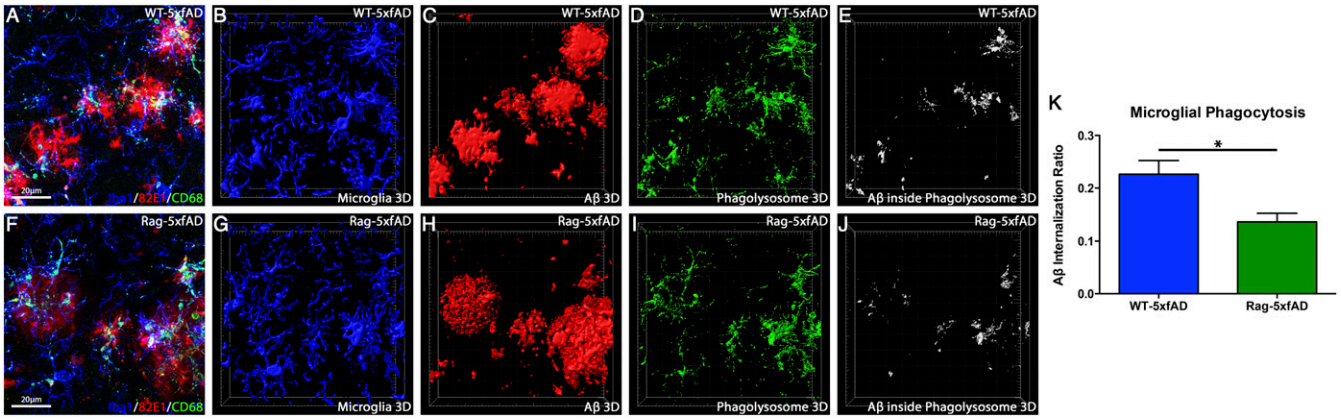

Fig. 4. Microglial phagocytosis is impaired in Rag-5xfAD mice. (*A* and *F*) Representative immunohistochemical images of microglia (Iba1), Aβ (82E1), and microglial phagolysosomes (CD68). (*B–E* and *G–J*) Three-dimensional reconstruction of microglia (blue; Iba1), Aβ (red; 82E1), phagolysosomes inside microglia (green; colocalization of CD68 and Iba1), and amyloid within phagolysosomes (white; colocalization of 82E1 and microglial phagolysosomes). (*K*) Calculation of the Aβ internalization ratio (Aβ within phagolysosomes, normalized to microglia number and total Aβ within the field) revealed a 39.6% decrease in Aβ internalization in Rag-5xfAD microglia compared with WT-5xfAD. Data are represented as mean ± SEM. Student's *t* test, $P < 0.05$; $n > 8$ animals/genotype.

increased in WT-5xfAD animals compared with WT-WT, no change was observed in Rag-5xfAD animals from basal Rag-WT levels, consistent with a lack of T-cell–derived IFNγ that would be expected in Rag mice (Fig. 3*K*). In addition to traditional proinflammatory cytokines, two recent studies demonstrated that the antiinflammatory cytokine interleukin 10 (IL-10) negatively regulates amyloid pathology (27, 28). We therefore also examined levels of IL-10 in all four groups. However, our analysis revealed no differences in IL-10 between Rag-5xfAD and WT-5xfAD (Fig. 3*L*), and thus, IL-10 is likely not responsible for the observed differences in Aβ in this model.

As microglial gene expression, morphology, and cytokine production were different in Rag-5xfAD mice, we wondered whether microglial phagocytosis of Aβ might also be altered. We therefore used high-power confocal *z*-stack imaging with IMARIS software colocalization, surface reconstruction, and volumetric quantification to analyze Aβ phagocytosis (28–30). Using this approach, we quantified the proportion of Aβ localized to microglial phagolysosomes and detected a nearly 39.6% decrease in phagocytic efficiency ($P = 0.016$) in Rag-5xfAD microglia vs. WT-5xfAD microglia (Fig. 4).

Elevated Levels of IgG Are Found in Association with Microglia in WT-5xfAD Mice. While examining immunolabeling with various mouse monoclonal antibodies in WT-5xfAD mice, we observed an unexpected but consistent pattern of microglial labeling. We hypothesized the labeling could be endogenous mouse Ig within the brain. We therefore used an anti-mouse f(ab′)2 fluorescently labeled secondary antibody to determine whether endogenous mouse IgG might be present within the WT-5xfAD brain. Indeed, we found significant immunolabeling of mouse IgG in association with Iba1+ microglia in WT-5xfAD brains (Fig. 5 *A–C*). In contrast, IgG labeling was greatly diminished in WT-WT mice (Fig. 5 *E–G*) and absent in Rag-5xfAD and Rag-WT mice (Fig. 5 *E–O*). Further examination of endogenous IgG labeling also revealed a high degree of labeling in the choroid plexus of both WT-WT and WT-5xfAD mice (Fig. 5 *D* and *H*). Although the choroid plexus can often exhibit nonspecific immunoreactivity, the specificity of this IgG labeling was confirmed by the absence of staining in the Rag-WT and Rag-5xfAD mice (Fig. 5 *L* and *P*). To further examine the differences in IgG levels between WT-5xfAD and WT-WT brains, we measured total mouse IgG within the brain and plasma by ELISA. Confirming our histological findings, we detected a significant 50% increase in IgG levels in the brains of WT-5xfAD vs. WT-WT mice (Fig. 6*A*). However, this difference was not due to an increase in peripheral IgG levels, as plasma IgG measurements revealed no differences between WT-WT and WT-5xfAD mice (Fig. 6*B*).

The observed increase in WT-5xfAD brain IgGs could be mediated by a breakdown in the blood–brain barrier (BBB), as recent studies have shown that the BBB can become disrupted in AD (31, 32). To determine whether this was the case, we used an Evans Blue permeability assay to assess BBB integrity (33) in all four genotypes. Interestingly, this experiment revealed no alterations in BBB permeability (Fig. S3 *A* and *B*); thus, IgG accumulates in the brains of WT-5xfAD by an alternative mechanism that currently remains unclear.

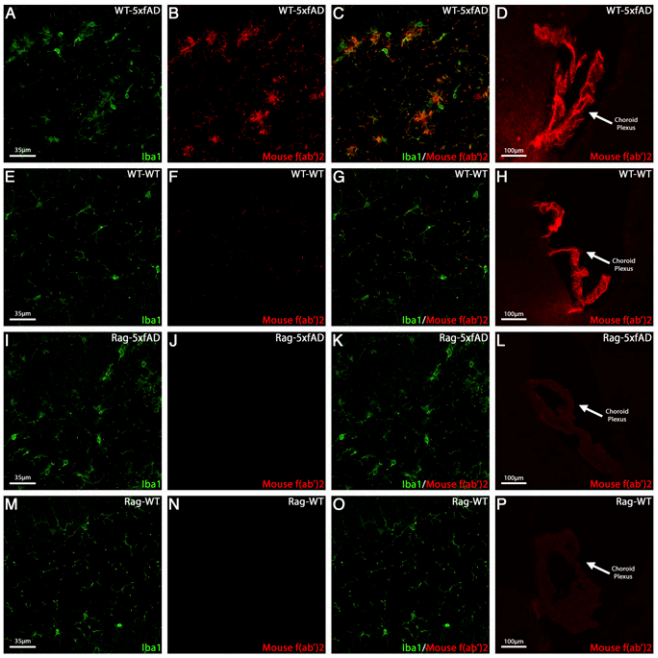

Fig. 5. Elevated levels of IgG are found in association with microglia in WT-5xfAD mice. (*A–C*) Representative immunohistochemical images showing that mouse IgG (red) is observed in close association with microglial membranes (green) in the brains of WT-5xfAD mice but not in WT-WT, Rag-WT, or Rag-5xfAD mice (*E–G*, *I–K*, and *M–O*). (*D* and *H*) The choroid plexus of WT-5xfAD and WT-WT both exhibit high levels of IgG. The specificity of the IgG labeling of choroid plexus is confirmed by the lack of labeling in Rag-5xfAD and Rag-WT mice (*L* and *P*).

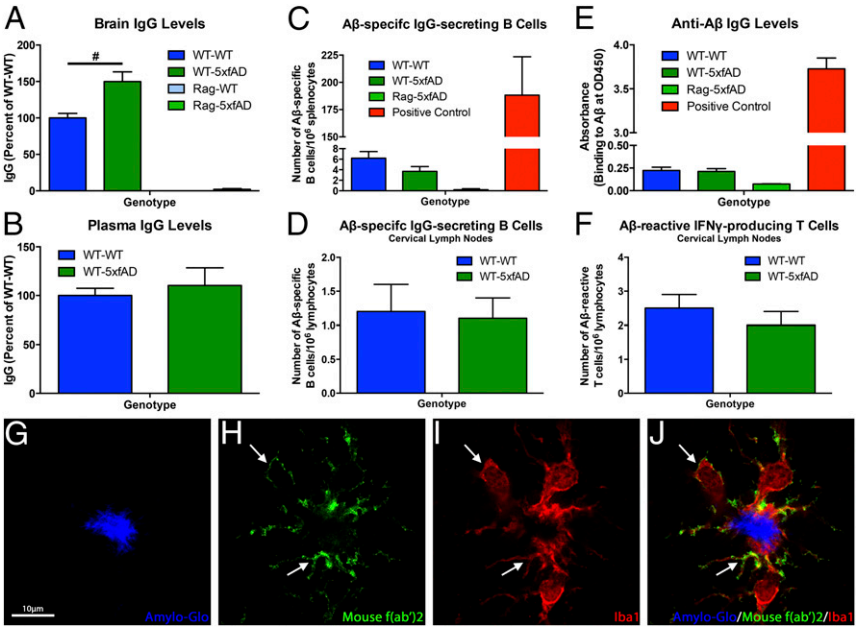

Fig. 6. WT-5xfAD mice exhibit increased total brain IgG but no Aβ-specific antibodies or Aβ-reactive B/T cells. (*A*) ELISA of soluble brain lysates confirms that WT-5xfAD mice exhibit significantly more brain IgG (~150%) compared with WT-WT mice. Unsurprisingly, no levels of IgG are observed in Rag-WT or Rag-5xfAD mice. (*B*) Despite the increase in brain IgG, no differences are observed between levels of peripheral IgG in plasma detected using the same ELISA. (*C–F*) Several assays demonstrate a lack of specific Aβ-reactive cells or anti-Aβ antibodies in WT-5xfAD compared with WT-WT. (*C*) ELISpot assay of splenocytes demonstrates background levels of Aβ-binding B cells within the spleen of WT-WT and WT-5xfAD mice; $n = 5$ animals/group. However, positive control mice receiving an active Aβ immunogen exhibit a very strong anti-Aβ B-cell response. (*D* and *F*) Analysis of lymphocytes isolated from the cervical lymph nodes (pooled deep and superficial) again find no difference in number of reactive cells between WT-WT and WT-5xfAD mice and that overall numbers of reactive cells are less than observed in splenocytes samples; $n = 10$ animals/group. (*E*) ELISA of sera collected from WT-WT, WT-5xfAD, and Rag-5xfAD mice demonstrates that equivalent background levels of Aβ-binding antibodies are detected in both WT-WT and WT-5xfAD mice, well below levels detected in mice receiving active Aβ immunization. (*G–J*) High-magnification confocal images further demonstrate a lack of IgG labeling of Aβ plaques, whereas surrounding Iba1+ microglial processes colabel with IgG. All data are represented as mean ± SEM. ANOVA, $P < 0.05$, and Fisher's PLSD post hoc, $^{\#}P < 0.001$.

WT-5xfAD Mice Lack Aβ-Specific B Cells and Anti-Aβ IgGs. To determine whether these endogenous IgGs were directed against Aβ, we collected sera from WT-WT, WT-5xfAD, and Rag-5xfAD mice and measured anti-Aβ antibody titers using a well-validated ELISA (34, 35). Despite testing extremely undiluted samples of sera, we found no differences between WT-WT and WT-5xfAD in levels of anti-Aβ IgG antibodies (Fig. 6*E*). In contrast, highly diluted samples taken from positive control mice that had been actively immunized against Aβ (red bar) exhibited a robust signal in this assay (Fig. 6*E*). Thus, neither WT-WT nor WT-5xfAD mice exhibit induction of anti-Aβ antibodies. To further confirm these results, we used a sensitive ELISpot assay to quantify numbers of anti-Aβ IgG producing B cells within the spleen. Using Rag-5xfAD mice that lack B cells as a negative control and mice actively immunized with Aβ peptide as a positive control, we detected no differences in anti-Aβ IgG producing B cells between WT-WT and WT-5xfAD splenocytes (Fig. 6*C*). As the immune response to a brain-localized antigen would be expected to be increased within the cervical lymph nodes, we next repeated this assay using cells extracted from the deep and superficial cervical lymph nodes. Analysis again revealed no differences between WT-WT and WT-5xfAD mice (Fig. 6*D*). We also performed an assay to determine whether WT-5xfAD mice exhibited a specific T-cell response to Aβ as indicated by IFNγ production following Aβ exposure. Similar to the B-cell ELISpot, this assay again revealed no differences in the reactivity of T cells to Aβ between genotypes (Fig. 6*F*). Last, further examination of brain IgG localization by high-magnification confocal microscopy confirmed that WT-5xfAD IgGs do not directly associate with amyloid plaques (Fig. 6 *G–J*) and instead colocalize with Iba1+ microglia, again suggesting that these brain-localized antibodies are not Aβ specific.

Preimmune Mouse IgG Induces Microglial Phagocytosis of Aβ. To further confirm the importance of brain-localized IgG in restraining Aβ pathology, we used Image Streamer flow cytometry to accurately quantify the effects of preimmune IgGs, purified from the sera of wild-type unimmunized mice, on microglial Aβ phagocytosis. Unlike standard flow cytometry, the Amnis Image Streamer system captures 256 fluorescent and phase-contrast images of cells as they pass through the system. On-board computer algorithms then calculate whether a given fluorescent signal is localized within the cell as opposed to being stuck to the outside membrane (Fig. 7*A*). Using this system, we examined whether the presence of preimmune mouse IgG could induce the phagocytosis of fibrillar fluorescently labeled Aβ by BV2 microglial cells. Cells were cultured in serum-free media and treated overnight with or without IL-1β to further mimic the proinflammatory state of the AD brain. Ten hours later, cells were exposed to fluorescently labeled fibrillized Aβ with or without preimmune IgGs for 1 h and then examined using the Image Streamer system. Interestingly, whereas relatively few cells phagocytosed Aβ following treatment with PBS/PBS, treatment with preimmune IgG induced a sixfold increase in the number of cells with internalized Aβ (Fig. 7 *A–C*). Furthermore, of those cells that did actively phagocytose Aβ, ones treated with IgG showed a twofold increase in the amount of Aβ phagocytosed as measured by mean fluorescence intensity within the cell (Fig. 7*D*). IL-1β/PBS pretreatment did not significantly change the amount of phagocytosis compared with PBS/PBS treatment. However, combined treatment of IL-1β/IgG significantly reduced the number of cells that phagocytosed Aβ vs. IgG alone, but slightly increased the amount of Aβ within those cells (Fig. 7 *C–E*), consistent with the known effects of IL-1β on microglial activation state and phagocytosis (36).

IgG Induces Aβ Phagocytosis via a Src/Syk/PI3K Signal Transduction Pathway. Next, we performed an additional in vitro experiment to determine the mechanism by which preimmune IgG activates phagocytic machinery to enhance Aβ clearance. IgG binding to Fc receptors can activate a signal transduction cascade that leads to membrane remodeling, actin reorganization, and the formation of a phagasome (reviewed in ref. 37). In macrophages and monocytes, this signaling pathway is initiated via phosphorylation of immunoreceptor tyrosine-based activation motifs (ITAMs) by enzymes of the Src tyrosine-kinase family and the subsequent docking and activation of spleen tyrosine kinase (Syk). This in turn activates Phosphatidylinositol 3-kinase (PI3K) and other downstream signaling pathways to induce phagosome formation. To determine whether IgG treatment of BV2 microglial cells activates this same canonical pathway, we pretreated BV2 cells with inhibitors of Src/Syk or PI3K and then exposed them to fluorescent Aβ and IgG for 30 min. Cells were then washed and fixed, and fluorescent Aβ in-

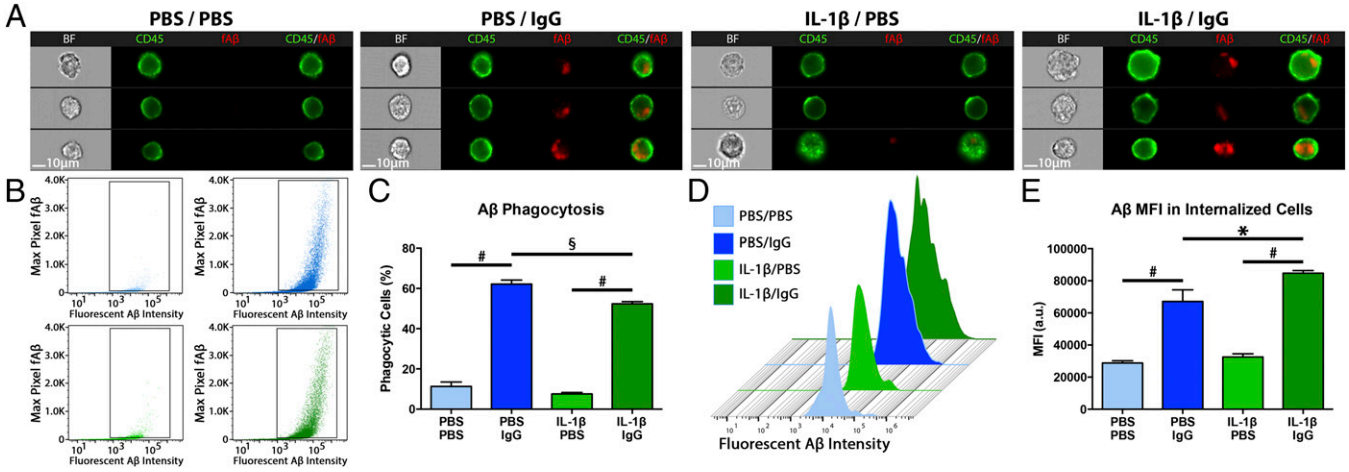

Fig. 7. Preimmune IgG is sufficient to induce robust Aβ phagocytosis. (*A*) Representative bright-field, and fluorescent images from Amnis Imagestreamer flow cytometry of fibrillar Aβ phagocytosis within BV2 microglial cells. (*B*) Raw data from phagocytosis flow cytometry demonstrating the gating of cells with internalized fluorescent fAβ (boxed regions). (*C*) Analysis of live BV2 cells with internalized Aβ demonstrates that addition of preimmune IgG induces a nearly sixfold increase in the percentage of cells that have phagocytosed Aβ. (*D*) Histogram of intensity of fluorescent Aβ only within cells that have internalized Aβ. (*E*) Amount of Aβ internalized within phagocytic cells illustrates that pretreatment with IgG increases the amount of amyloid internalized by over twofold on average. Interestingly, pretreatment of cells with IL-1β significantly reduces the number of phagocytic cells, but increases the amount of Aβ they engulf. Data are represented as mean ± SEM. ANOVA, $P < 0.05$, and Fisher's PLSD post hoc, $^{*}P < 0.05$, $^{\S}P < 0.01$, $^{\#}P < 0.001$; $n = 6$ wells/group.

ternalization was imaged and quantified by a blinded observer. As before, we again found that treatment with preimmune IgGs dramatically increases Aβ phagocytosis (Fig. S4). In contrast, pretreatment with a selective inhibitor of Src and Syk tyrosine kinases [3,4-methylenedioxy-β-nitrostyrene (MNS)] or the PI3K inhibitor wortmannin, completely abrogated Aβ phagocytosis (Fig. S4). Thus, it appears that IgG-induced uptake of Aβ by microglial cells involves activation of Src/Syk/PI3K phagocytosis signal transduction pathways.

Preimmune Mouse IgG Reduces Aβ Plaque Load in Vivo. Consistent with our in vitro analysis, previous studies have demonstrated that injection of preimmune IgG into the brain of a different transgenic AD model can promote Aβ clearance (38). To determine whether a similar approach can reduce Aβ in a mouse model that lacks B, T, and NK cells, we replicated this design by stereotactically injecting preimmune IgG (2 μL of 1 mg/mL) into one hippocampus and PBS into the contralateral hippocampus of Rag-5xfAD mice. Seven days later, mice were killed, and amyloid burden was assessed, revealing a significant reduction in Aβ plaque volume by 50.9% ($P = 0.01$) on the IgG-injected side (Fig. S5 *A*–*C*). Further subanalysis demonstrated that IgG delivery also significantly reduced the number of large plaques ($P = 0.01$; Fig. S5*D*).

Bone Marrow Adoptive Transfer Reduces Aβ Pathology in Rag-5xfAD Mice. To determine whether replacing the missing adaptive immune cell populations in the periphery could also reverse the effects of immune deficiency on AD pathology, adoptive transfer of whole bone marrow was performed. At 2 mo of age, Rag-5xfAD mice received an injection of either 500,000 whole bone marrow cells from age- and sex-matched immune-intact WT-5xfAD mice or an equivalent injection of vehicle into the retroorbital venous sinus. Mice were allowed to age normally for 4 mo, and then brains were processed for analysis. Successful engraftment was confirmed by flow-cytometric analysis of splenocytes at the time of killing (Fig. S6 *A* and *B*). Next, using both biochemical and histological endpoints, we assessed the impact of bone marrow transplantation on Aβ pathology. Immunohistochemical analysis of hippocampal amyloid burden revealed a significant 47.4% reduction in plaque volume in mice that received bone marrow transplants ($P < 0.05$; Fig. 8 *A*–*C*). Subanalysis of plaque load demonstrated that numbers of both medium and large plaques were significantly reduced with bone marrow transplantation ($P < 0.05$) and numbers of small plaques were almost significantly decreased ($P = 0.056$) (Fig. 8*D*). To confirm our immunohistochemical analysis, we followed up with ELISA measurement of Aβ and detected a significant reduction in Aβ40 and nearly a significant reduction in Aβ38 ($P = 0.058$) (Fig. 8*E*). To determine whether endogenous mouse IgG was present in the brain following bone marrow engraftment, we also examined mouse IgG levels by ELISA and immunohistochemistry. These analyses confirmed that replacement of peripheral immune cells could elevate levels of IgG within the brain (Fig. 8*F*) and likewise led to the characteristic colabeling of microglia with endogenous mouse IgG (Fig. 8 *G*–*N*). Taken together, these data strongly implicate adaptive immunity, the production of IgGs, and cross talk between peripheral and central immune systems as being critical for regulating and restraining the development of AD pathology.

Discussion

Although the role of the brain's innate immune cells, microglia, in AD has been extensively examined, the influence of peripheral immune cell populations in this disease has been underexplored. In the current study, we sought to address this by creating a novel immune-deficient model of AD. The resulting Rag-5xfAD mice lack B, T, and NK cells and develop aggressive AD-like neuropathology. Most interestingly, we find that deletion of these peripheral immune populations leads to a greater than twofold increase in amyloid burden. Similar to sporadic AD patients, our data reveal that the increase in pathology is not driven by altered Aβ production, but likely via impaired clearance (23–25). To better understand precisely how Aβ clearance is decreased in Rag-5xfAD mice, we used unbiased GO analysis, which implicated microglia function and changes in both adaptive and innate immunity.

The detection of IgGs within the brains of immune-intact AD transgenics suggested that antibody-mediated clearance mechanisms may be involved. Interestingly, we find that, although immune-intact 5xfAD mice exhibit IgGs within their brain, these antibodies and the B cells that produce them are not specific for Aβ. Rather, our data reveal that non–Aβ-specific antibodies can significantly enhance the phagocytosis of Aβ fibrils by activating Src/Syk/PI3K phagocytic signaling pathways. Furthermore, delivery of IgG to Rag-5xfAD

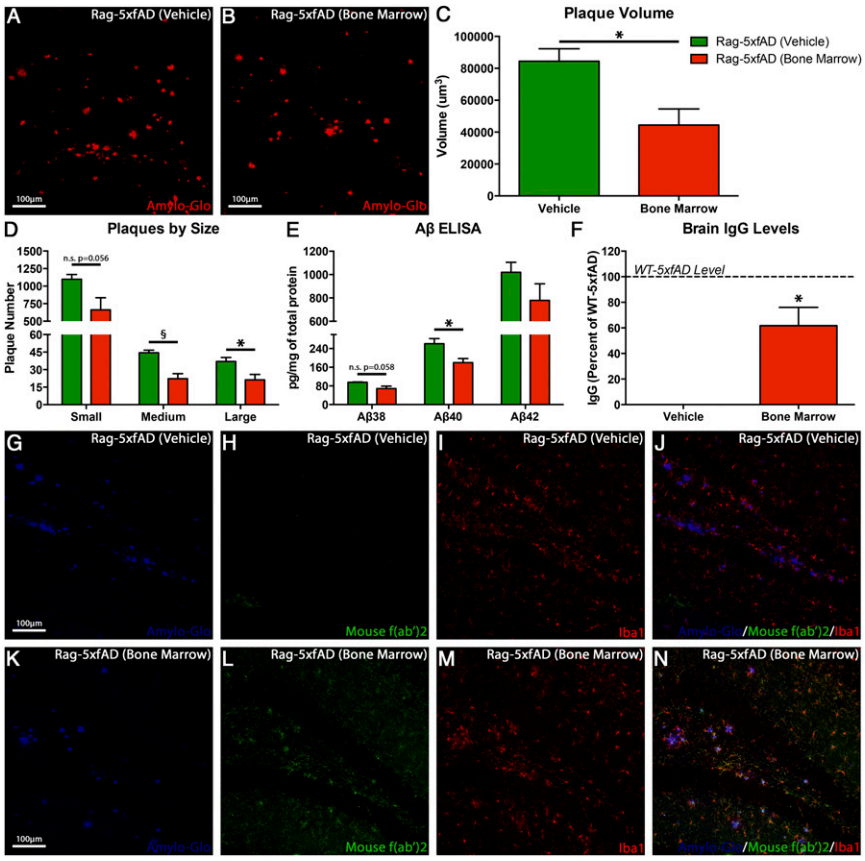

Fig. 8. Bone marrow transplantation reduces amyloid in Rag-5xfAD mice. (*A* and *B*) Representative immunohistochemical images demonstrate a significant reduction in amyloid burden in the dentate gyrus of animals receiving bone marrow (*B*) compared with those receiving vehicle injections (*A*). (*C* and *D*) IMARIS-based 3D quantification of Aβ confirms a reduction in both total Aβ volume and the numbers of medium and small plaques ($P < 0.05$). The number of small plaques trended lower in bone marrow-treated animals ($P = 0.056$). (*E*) Multiplex ELISA confirmed the IHC findings as Aβ40 was significantly reduced, and Aβ38 and Aβ42 trended down as well. (*F*) ELISA analysis of brain IgG levels demonstrated elevated levels in mice receiving bone marrow, although not quite at the same levels as WT-5xfAD mice. (*G–N*) Importantly, bone marrow-treated Rag-5xfAD mice also exhibit similar and extensive immunohistochemical labeling of microglia with IgG, as described above in WT-5xfAD mice (Fig. 5). Unsurprisingly, this labeling was absent in mice receiving vehicle injections. Data are represented as mean ± SEM. ANOVA, $P < 0.05$, and Fisher's PLSD post hoc, $^{*}P < 0.05$, $^{\S}P < 0.01$; *N*, 4–5 per group.

mice by either direct stereotactic injection or peripherally via bone marrow transplantation leads to a corresponding decrease in Aβ.

Previous reports have implicated a role for non–Aβ-specific antibodies in Aβ clearance. For example, Gammagard, a formulation of human immunoglobulins, has been tested in both AD models and patients (39, 40). In mouse models, these studies have shown that IgGs can reduce Aβ levels especially when directly injected into the brain (38, 41), and our own data have confirmed these findings. However, despite promising phase II results, a phase III clinical trial of Gammagard in mild-to-moderate AD patients failed to improve cognition. However, Gammagard did significantly reduce Aβ levels and slow cognitive decline in a preplanned subgroup analysis of patients carrying the ApoE4 risk allele (39, 40). Further support for the potential influence of peripheral IgG in the clearance of Aβ pathology has recently been suggested by a group that used transcranial focused ultrasound to transiently open the BBB. Following ultrasound, this group observed a significant reduction in amyloid pathology, which they suggested might be due to increased infiltration of endogenous IgG into the brain (42, 43).

Although the lack of cognitive improvement in the Gammagard trials is discouraging, there is a growing consensus that AD will likely have to be tackled during the prodromal phase with primary or secondary prevention trials, as even Aβ-targeting antibodies have failed to improve cognition in phase III trials (44, 45). It is therefore quite possible that Gammagard or other IgG formulations, perhaps combined with transient permeabilization of the BBB through focused ultrasound, might provide increased benefit if tested in prodromal AD.

One disease that dramatically affects the adaptive immune system is HIV/AIDS. Before the advent of antiretroviral therapies, dementia was a common cause of morbidity in HIV, affecting up to 50% of patients (46). Furthermore, Aβ accumulation within the brain and changes in cerebrospinal fluid Aβ levels that mimic AD are observed in these patients and correlate well with cognitive dysfunction (47, 48). Although HIV primarily targets CD4 T-helper populations, these cells play a critical role in the induction of Ig class switching by B cells and the maturation of B cells into IgG-producing plasma cells (49). It is therefore interesting to speculate that, as in our immune-deficient AD mouse model, immunodeficiency in humans might likewise impair the clearance of Aβ from the brain.

An important question is how the current data fit with a recent study examining the effects of Tregs on AD pathogenesis (17). Tregs normally serve to suppress the systemic immune system and protect against autoimmune disease (50). However, in AD mouse models, it appears that this immunosuppressive activity may be detrimental, impairing the ability of the adaptive immune system to respond to and restrain Aβ pathology. When Tregs are depleted for example, Aβ pathology decreased dramatically, whereas compounds that promote Treg differentiation and function exacerbate pathology (17). In comparison, Rag-5xfAD mice lack not only Tregs but also many other components of the adaptive immune system including CD4 and CD8 T cells, B cells, and plasma cells. These other components are many of the target cells that Tregs serve to restrain; thus, deletion of all of these populations in Rag-5xfAD mice produces an effect that is very similar to the effect produced by promoting Treg function. It therefore appears that the current study and this recent report on Tregs support a similar conclusion about the importance of peripheral leukocyte populations in restraining AD pathology.

It is important to acknowledge some potential caveats regarding the interpretation of the current study. Perhaps the most important is that the Rag-5xfAD mice may exhibit some inherent developmental differences in microglial function. However, no changes in microglial number, cytokine levels, and gene expression profiles between WT-WT and Rag-WT mice were observed. Only a small but significant difference in microglial morphology between these

two groups exists (Figs. 2*D* and 3 *F* and *G*, and Dataset S1). Together, these data suggest that, if any potential developmental effects of adaptive immune system ablation on microglial function are present, they are subtle and only manifest in an environment necessitating adaptive–innate immunity cross talk such as in response to a robust insult such as Aβ accumulation.

Another interesting question that remains is precisely how IgG levels become elevated in WT-5xfAD brains. Only 0.1% of circulating IgGs reach the brain in wild-type mice by passive diffusion (51, 52). Because no apparent increase in BBB permeability was detected in 5xfAD mice, other routes for IgG entry may be important. Recent evidence has implicated the choroid plexus as a gateway for immune signals reaching the brain (53, 54), and in support of this hypothesis, high levels of IgG were present within the choroid plexus of immune-intact mice. Emerging evidence implicates choroid plexus dysfunction in AD (55, 56). Thus, it is possible that the choroid plexus regulates the influx of IgG into the brain. Alternatively, increased association with microglial Fc receptors or decreased clearance of IgGs from the brain might also play a role in the observed IgG elevations (57, 58).

Taken together, our data reveal a significant and previously unidentified role for the adaptive immune system in AD pathogenesis. Not only does the loss of B, T, and NK cells substantially accelerate amyloid pathogenesis, but it also exacerbates the neuroinflammatory phenotype of microglia while decreasing phagocytic activity. One mechanism by which these peripheral cell populations exert their effect is through the production of IgGs. Our data confirm that IgG alone is sufficient to increase phagocytosis in vitro and that delivery of IgG directly to the brains of Rag-5xfAD mice or into circulation via adoptive transfer can induce plaque clearance. Our study therefore adds to a growing area of research that highlights the importance of the peripheral immune system in CNS function and AD (17, 18), and demonstrates the need to better understand how these peripheral cell populations act in concert with microglia to influence the CNS in both normal and diseased conditions.

Materials and Methods

Animals. All animal procedures were performed in strict accordance to the guidelines of the National Institutes of Health and University of California Institutional Animal Care and Use Committee. The Rag-5xfAD immune-deficient AD mouse model was created by backcrossing 5xFAD transgenic mice onto a Rag2/il2rγ double-knockout background. Briefly, 5xfAD mice (MMRRC strain: 034848-JAX) express two cointegrated and coinherited transgenes (APP and PS-1). The APP transgene includes three familial AD mutations (Swedish, Florida, London), and the PS-1 transgene includes two mutations (M146L and L286V) (19). Purebred C57Bl6 5xfAD mice were crossed with Rag2/il2rγ double-knockout mice (Taconic; 4111) (59), followed by repeated littermate crosses from each generation (Fig. S1*A*), to create mice that are heterozygous for the APP/PS-1 transgenes and lack both copies of the Rag2 and Il2rγ genes (Il2rγ −/y in males). We also simultaneously generated strain-matched immune-deficient mice wild type for the AD transgenes hereafter referred to as Rag-WT, as well as strain-matched immune-competent AD and WT mice referred to as WT-5xfAD and WT-WT, respectively. Sex- and age-matched mice were used, and all animals were group housed on a 12-h/12-h light/dark cycle with access to food and water ad libitum.

Immunohistochemistry. Fluorescent immunohistochemical analysis followed previously described established protocols (60). Primary antibodies used for immunohistochemical analysis included the following: Iba1 (Wako), Iba1 (Abcam), CD68 (Abcam), Aβ40 (Life Technologies), Aβ42 (Life Technologies), 82E1 (IBL America), GFAP (Millipore), f(ab′)2 fragment of goat anti-mouse IgG directly conjugated to Alexa Fluor 488 or 555 (Life Technologies). Sections were incubated in primary antibodies overnight followed by detection with appropriate Alexa Fluor-conjugated secondary antibody (Life Technologies) and coverslipped using Fluoromount-G with or without DAPI (Southern Biotech). Fibrillar amyloid was visualized using Amylo-Glo (Biosensis) diluted 1:100 in 0.01 M PBS (61).

Confocal Microscopy and Quantitative Analysis. Immunofluorescent sections were visualized, and images were captured using an Olympus FX1200 confocal microscope. Aβ plaques were quantified using the Surfaces function followed by volume analysis in IMARIS software (Bitplane). IMARIS-based quantification of microglial number, morphology, and Aβ phagocytosis followed previously described methods using the Colocalization and Surfaces functions (28–30, 33). To calculate Aβ internalization ratio, the volume of Aβ within $CD68^+$ phagolysosomes was normalized to microglia number and total Aβ volume within the field. All images were captured and analyzed by a blind observer using coded slides.

Affymetrix Transcriptome Array. mRNA was extracted from frozen half-brains using RNA Plus Universal Mini Kit (Qiagen), and sample purity and concentration were verified by Bioanalyzer (Agilent). Affymetrix GeneChip Mouse Transcriptome 1.0 arrays were then used to collect global transcriptional profiles in 16 samples (4 per group) by the University of California, Irvine (UCI) Genomics High-Throughput Facility. Background correction and normalization of raw data were conducted via robust multiarray analysis algorithm implemented in Bioconductor package "oligo 1.32." All samples passed quality control analysis. Additionally, array features were filtered with Bioconductor packages "genefilter 1.50" and "mta10sttranscriptcluster.db 8.3.1" for Entrez IDs resulting in ∼24,600 genes for further analysis.

Unsupervised Hierarchical Clustering, Functional Enrichment, and GO. Unsupervised hierarchical clustering (R packages flashClust 1.01-2 and gplots 2.17) were performed on subsets of genes that have previously been shown to be enriched in microglia or neurons (26). Differentially expressed genes (DEGs) were determined between all contrasts of genotypes, and multiple testing was done with Benjamini–Hochberg method to obtain the corresponding |logFC| and *P* value implemented in Bioconductor package "limma 3.24.25." Genes with adjusted *P* value of <0.01 were used for constructing Venn diagram (JMP Pro-11.2 software) and GO analyses. Bioconductor packages "topGO 20.2," "GO.db 3.1.2," and "gage 2.18" were used to perform GO enrichment for the DEGs found significant in Rag5xfAD vs. WT5xfAD contrast. $P < 0.05$ was defined as the cutoff to identify the statistical significance of enrichment analyses.

IgG and B-Cell/T-Cell Reactivity by ELISA and ELISPOT. Blood was collected from retroorbital sinus, and titers of anti-Aβ antibodies in mouse sera were determined by ELISA as previously described (34, 35). Spleens, deep cervical lymph nodes (DCLNs), and superficial cervical lymph nodes (SCLNs) were collected, and antibody-forming B cells specific to Aβ were detected in splenocytes and pooled DCLN/SCLN lymphocytes by ELISPOT (Mabtech). Splenocytes or lymphocytes were incubated for 24 h in 96-well plates coated with Aβ peptide, and the assay was performed following manufacturer's protocol (Mabtech). Sera and splenocytes were also collected from mice immunized with Aβ as a positive control (34, 35). Analysis of IFNγ production by T cells was performed in DCLN/SCLN lymphocytes by ELISpot assay (BD Biosciences). Cultures of lymph node cells were restimulated in vitro with soluble Aβ (10 μg/mL) for 20 h. The numbers of spot-forming cells per 10^6 lymph node cells stimulated with Aβ were then counted.

In Vitro Phagocytosis Assay. Phagocytosis was assessed following previous methods with some modifications (36, 62). First, BV2 cells (63) (3.0×10^5 cells per well) were exposed to either proinflammatory cytokine IL-1β (20 ng/mL; Thermo Fisher Scientific) or 0.1% BSA in PBS for 10–12 h. After IL-1β or PBS preexposure, the cells were changed to serum-free DMEM and then exposed to $fA\beta_{1-42}$ (10 μg/mL) with murine IgG (0.5 mg/mL; Jackson ImmunoResearch Laboratories) or PBS for 1 h at 37 °C. Next, the cells were washed three times with prewarmed PBS to remove unassociated $fA\beta_{1-42}$. Cold PBS was added to wells, and the cells were collected, centrifuged (5 min, 600 × *g*), washed in PBS, and suspended in flow cytometer buffer (PBS with 0.1% BSA and 0.5 mM EDTA) and placed on ice. BV2 cells were incubated with rat anti-CD16/32 Fc receptor block (2 mg/mL; BD Biosciences) for 5 min at 4 °C. Cells were then stained with anti–CD45-APC clone 30-F11 (Tonbo Biosciences) at 1:200 in flow cytometer buffer. Samples were then analyzed using Amnis Imagestreamer^x Mark II Imaging Flow Cytometer (Millipore). $fA\beta_{1-42}$ phagocytosis was analyzed using the IDEAS software onboard Internalization Wizard algorithm. Figures represent single cells that internalized $fA\beta_{1-42}$ from each group ($n = 6$) with mean and SE reported.

Bone Marrow Adoptive Transfer. Age- and sex-matched immune intact 5xfAD mice served as donors for bone marrow adoptive transfer. Donor mice were killed by CO_2 asphyxiation, femurs were removed, and whole bone marrow was harvested by flushing the marrow contents with PBS. Marrow was then treated with ammonium chloride–potassium buffer to lyse red blood cells, filtered through a 70-μm nylon mesh, and cell numbers were counted by hemocytometer. Each recipient (n = 4–5 females/group) was anesthetized with isoflurane before receiving 500,000 live cells in 100 μL or

equivalent volume of PBS via retroorbital injection. To confirm engraftment, at the time of killing, splenocytes were collected and analyzed for the presence of B, T, and NK cells by flow cytometry as described in *SI Materials and Methods*.

***SI Materials and Methods*.** Detailed descriptions of all other standard experimental procedures, including tissue processing, flow cytometry, Western blot, ELISA, Evans Blue assay, qPCR, cell culture, Aβ preparation, phagocytosis inhibition, intracranial IgG injection, and statistical analysis, can be found in *SI Materials and Methods*.

ACKNOWLEDGMENTS. We thank the University of California, Irvine Genomics High-Throughput Facility for performing the Mouse Transcriptome 1.0 Array. Special thanks to Andy Agazaryan and Joy Davis for assistance with establishment of the Rag-5xfAD model. We also thank the Institute for Immunology and Drs. Eric Pearlman and Jennifer Atwood for assistance with Amnis Image streamer, and the National Institute of Allergy and Infectious Disease for contributing the C57BL/6J × C57BL/10SgSnAi)-(KO) γc-(KO)*Rag2* mice to Taconic. Thanks also to Laura McIntyre and Dr. Craig Walsh for assistance in isolation of cervical lymph nodes. This work was supported by NIH Grant RF1AG048099 (to M.B.-J.), Alzheimer's Association Grant BFG-14-317000 (to M.B.-J.), NIH Grant P50 AG016573 (to W.W.P. and M.B.-J.), NIA Grant T32 AG00096-30 (to S.E.M.), and NINDS Grant T32 NS082174-01 (to S.E.M.).

1. Alzheimer's Association (2014) 2014 Alzheimer's disease facts and figures. *Alzheimers Dement* 10(2):e47–e92.
2. McAlpine FE, Tansey MG (2008) Neuroinflammation and tumor necrosis factor signaling in the pathophysiology of Alzheimer's disease. *J Inflamm Res* 1:29–39.
3. Maier M, et al. (2008) Complement C3 deficiency leads to accelerated amyloid beta plaque deposition and neurodegeneration and modulation of the microglia/macrophage phenotype in amyloid precursor protein transgenic mice. *J Neurosci* 28(25):6333–6341.
4. Wyss-Coray T, Rogers J (2012) Inflammation in Alzheimer disease—a brief review of the basic science and clinical literature. *Cold Spring Harb Perspect Med* 2(1):a006346.
5. Guillot-Sestier MV, Town T (2013) Innate immunity in Alzheimer's disease: A complex affair. *CNS Neurol Disord Drug Targets* 12(5):593–607.
6. Lee CY, Landreth GE (2010) The role of microglia in amyloid clearance from the AD brain. *J Neural Transm (Vienna)* 117(8):949–960.
7. Mosher KI, Wyss-Coray T (2014) Microglial dysfunction in brain aging and Alzheimer's disease. *Biochem Pharmacol* 88(4):594–604.
8. Heneka MT, et al. (2015) Neuroinflammation in Alzheimer's disease. *Lancet Neurol* 14(4):388–405.
9. Hickman SE, Allison EK, El Khoury J (2008) Microglial dysfunction and defective beta-amyloid clearance pathways in aging Alzheimer's disease mice. *J Neurosci* 28(33):8354–8360.
10. Krabbe G, et al. (2013) Functional impairment of microglia coincides with beta-amyloid deposition in mice with Alzheimer-like pathology. *PLoS One* 8(4):e60921.
11. Bradshaw EM, et al.; Alzheimer Disease Neuroimaging Initiative (2013) CD33 Alzheimer's disease locus: Altered monocyte function and amyloid biology. *Nat Neurosci* 16(7):848–850.
12. Griciuc A, et al. (2013) Alzheimer's disease risk gene CD33 inhibits microglial uptake of amyloid beta. *Neuron* 78(4):631–643.
13. Guerreiro R, et al.; Alzheimer Genetic Analysis Group (2013) TREM2 variants in Alzheimer's disease. *N Engl J Med* 368(2):117–127.
14. Jay TR, et al. (2015) TREM2 deficiency eliminates TREM2+ inflammatory macrophages and ameliorates pathology in Alzheimer's disease mouse models. *J Exp Med* 212(3):287–295.
15. Wang Y, et al. (2015) TREM2 lipid sensing sustains the microglial response in an Alzheimer's disease model. *Cell* 160(6):1061–1071.
16. Pellicanò M, et al. (2012) Immune profiling of Alzheimer patients. *J Neuroimmunol* 242(1-2):52–59.
17. Baruch K, et al. (2015) Breaking immune tolerance by targeting Foxp3(+) regulatory T cells mitigates Alzheimer's disease pathology. *Nat Commun* 6:7967.
18. Zenaro E, et al. (2015) Neutrophils promote Alzheimer's disease-like pathology and cognitive decline via LFA-1 integrin. *Nat Med* 21(8):880–886.
19. Oakley H, et al. (2006) Intraneuronal beta-amyloid aggregates, neurodegeneration, and neuron loss in transgenic mice with five familial Alzheimer's disease mutations: Potential factors in amyloid plaque formation. *J Neurosci* 26(40):10129–10140.
20. Dranoff G (2004) Cytokines in cancer pathogenesis and cancer therapy. *Nat Rev Cancer* 4(1):11–22.
21. Reiman EM, et al. (2012) Brain imaging and fluid biomarker analysis in young adults at genetic risk for autosomal dominant Alzheimer's disease in the presenilin 1 E280A kindred: A case-control study. *Lancet Neurol* 11(12):1048–1056.
22. Potter R, et al. (2013) Increased in vivo amyloid-β42 production, exchange, and loss in presenilin mutation carriers. *Sci Transl Med* 5(189):189ra77.
23. Mawuenyega KG, et al. (2010) Decreased clearance of CNS beta-amyloid in Alzheimer's disease. *Science* 330(6012):1774.
24. Wildsmith KR, Holley M, Savage JC, Skerrett R, Landreth GE (2013) Evidence for impaired amyloid β clearance in Alzheimer's disease. *Alzheimers Res Ther* 5(4):33.
25. Tarasoff-Conway JM, et al. (2015) Clearance systems in the brain—implications for Alzheimer disease. *Nat Rev Neurol* 11(8):457–470.
26. Zhang Y, et al. (2014) An RNA-sequencing transcriptome and splicing database of glia, neurons, and vascular cells of the cerebral cortex. *J Neurosci* 34(36):11929–11947.
27. Chakrabarty P, et al. (2015) IL-10 alters immunoproteostasis in APP mice, increasing plaque burden and worsening cognitive behavior. *Neuron* 85(3):519–533.
28. Guillot-Sestier MV, et al. (2015) Il10 deficiency rebalances innate immunity to mitigate Alzheimer-like pathology. *Neuron* 85(3):534–548.
29. Guillot-Sestier MV, Doty KR, Town T (2015) Innate immunity fights Alzheimer's disease. *Trends Neurosci* 38(11):674–681.
30. Leinenga G, Götz J (2015) Scanning ultrasound removes amyloid-β and restores memory in an Alzheimer's disease mouse model. *Sci Transl Med* 7(278):278ra33.
31. Deane R, et al. (2008) apoE isoform-specific disruption of amyloid beta peptide clearance from mouse brain. *J Clin Invest* 118(12):4002–4013.
32. Zlokovic BV (2013) Cerebrovascular effects of apolipoprotein E: Implications for Alzheimer disease. *JAMA Neurol* 70(4):440–444.
33. Elmore MR, et al. (2014) Colony-stimulating factor 1 receptor signaling is necessary for microglia viability, unmasking a microglia progenitor cell in the adult brain. *Neuron* 82(2):380–397.
34. Davtyan H, et al. (2010) DNA prime-protein boost increased the titer, avidity and persistence of anti-Abeta antibodies in wild-type mice. *Gene Ther* 17(2):261–271.
35. Davtyan H, Petrushina I, Ghochikyan A (2014) Immunotherapy for Alzheimer's disease: DNA- and protein-based epitope vaccines. *Methods Mol Biol* 1143:259–281.
36. Koenigsknecht-Talboo J, Landreth GE (2005) Microglial phagocytosis induced by fibrillar beta-amyloid and IgGs are differentially regulated by proinflammatory cytokines. *J Neurosci* 25(36):8240–8249.
37. García-García E, Rosales C (2002) Signal transduction during Fc receptor-mediated phagocytosis. *J Leukoc Biol* 72(6):1092–1108.
38. Sudduth TL, Greenstein A, Wilcock DM (2013) Intracranial injection of Gammagard, a human IVIg, modulates the inflammatory response of the brain and lowers Aβ in APP/PS1 mice along a different time course than anti-Aβ antibodies. *J Neurosci* 33(23):9684–9692.
39. Knight EM, Gandy S (2014) Immunomodulation and AD—down but not out. *J Clin Immunol* 34(Suppl 1):S70–S73.
40. Relkin N (2014) Clinical trials of intravenous immunoglobulin for Alzheimer's disease. *J Clin Immunol* 34(Suppl 1):S74–S79.
41. Counts SE, et al. (2014) Intravenous immunoglobulin (IVIG) treatment exerts antioxidant and neuropreservatory effects in preclinical models of Alzheimer's disease. *J Clin Immunol* 34(Suppl 1):S80–S85.
42. Jordão JF, et al. (2013) Amyloid-β plaque reduction, endogenous antibody delivery and glial activation by brain-targeted, transcranial focused ultrasound. *Exp Neurol* 248:16–29.
43. Burgess A, et al. (2014) Alzheimer disease in a mouse model: MR imaging-guided focused ultrasound targeted to the hippocampus opens the blood-brain barrier and improves pathologic abnormalities and behavior. *Radiology* 273(3):736–745.
44. Carrillo MC, et al. (2013) Can we prevent Alzheimer's disease? Secondary "prevention" trials in Alzheimer's disease. *Alzheimers Dement* 9(2):123–131.e1.
45. Liu E, et al.; Bapineuzumab 301 and 302 Clinical Trial Investigators (2015) Amyloid-β ^{11}C-PiB-PET imaging results from 2 randomized bapineuzumab phase 3 AD trials. *Neurology* 85(8):692–700.
46. Ances BM, Ellis RJ (2007) Dementia and neurocognitive disorders due to HIV-1 infection. *Semin Neurol* 27(1):86–92.
47. Brew BJ, Pemberton L, Blennow K, Wallin A, Hagberg L (2005) CSF amyloid beta42 and tau levels correlate with AIDS dementia complex. *Neurology* 65(9):1490–1492.
48. Soontornniyomkij V, et al. (2012) Cerebral β-amyloid deposition predicts HIV-associated neurocognitive disorders in APOE ε4 carriers. *AIDS* 26(18):2327–2335.
49. Xu W, Banchereau J (2014) The antigen presenting cells instruct plasma cell differentiation. *Front Immunol* 4:504.
50. Sakaguchi S, Yamaguchi T, Nomura T, Ono M (2008) Regulatory T cells and immune tolerance. *Cell* 133(5):775–787.
51. Poduslo JF, Curran GL, Berg CT (1994) Macromolecular permeability across the blood–nerve and blood–brain barriers. *Proc Natl Acad Sci USA* 91(12):5705–5709.
52. Fuller JP, Stavenhagen JB, Teeling JL (2014) New roles for Fc receptors in neurodegeneration-the impact on immunotherapy for Alzheimer's disease. *Front Neurosci* 8:235.
53. Ransohoff RM, Engelhardt B (2012) The anatomical and cellular basis of immune surveillance in the central nervous system. *Nat Rev Immunol* 12(9):623–635.
54. Schwartz M, Baruch K (2014) The resolution of neuroinflammation in neurodegeneration: Leukocyte recruitment via the choroid plexus. *EMBO J* 33(1):7–22.
55. Baruch K, et al. (2014) Aging. Aging-induced type I interferon response at the choroid plexus negatively affects brain function. *Science* 346(6205):89–93.
56. Bergen AA, Kaing S, Ten Brink JB, Gorgels TG, Janssen SF; Netherlands Brain Bank (2015) Gene expression and functional annotation of human choroid plexus epithelium failure in Alzheimer's disease. *BMC Genomics* 16(1):956.
57. Schlachetzki F, Zhu C, Pardridge WM (2002) Expression of the neonatal Fc receptor (FcRn) at the blood-brain barrier. *J Neurochem* 81(1):203–206.
58. Deane R, et al. (2005) IgG-assisted age-dependent clearance of Alzheimer's amyloid beta peptide by the blood-brain barrier neonatal Fc receptor. *J Neurosci* 25(50):11495–11503.
59. Cao X, et al. (1995) Defective lymphoid development in mice lacking expression of the common cytokine receptor gamma chain. *Immunity* 2(3):223–238.
60. Blurton-Jones M, et al. (2009) Neural stem cells improve cognition via BDNF in a transgenic model of Alzheimer disease. *Proc Natl Acad Sci USA* 106(32):13594–13599.
61. Schmued L, et al. (2012) Introducing Amylo-Glo, a novel fluorescent amyloid specific histochemical tracer especially suited for multiple labeling and large scale quantification studies. *J Neurosci Methods* 209(1):120–126.
62. Webster SD, et al. (2001) Antibody-mediated phagocytosis of the amyloid beta-peptide in microglia is differentially modulated by C1q. *J Immunol* 166(12):7496–7503.
63. Blasi E, Barluzzi R, Bocchini V, Mazzolla R, Bistoni F (1990) Immortalization of murine microglial cells by a v-raf/v-myc carrying retrovirus. *J Neuroimmunol* 27(2-3):229–237.

Supporting Information

Marsh et al. 10.1073/pnas.1525466113

SI Materials and Methods

Tissue Processing. At 7 mo of age, mice were anesthetized with Euthasol before intracardial perfusion with 0.01 M PBS. Immediately following perfusion, brains were quickly removed, and hemispheres were separated. The cerebellum was removed from the right hemisphere and then immediately flash-frozen in dry ice for subsequent biochemical analysis. The left hemisphere was drop-fixed in 4% (wt/vol) paraformaldehyde for 48 h at 4 °C. After 48-h fixation, the left hemispheres were transferred to 0.01 M PBS and 0.02% NaN_3 for storage until sectioning. Brains were sectioned coronally on a freezing microtome at 40-μm thickness.

Biochemical Tissue Processing. Right hemispheres, previously frozen on dry ice and stored at −80 °C, were crushed on dry ice using mortar and pestle. Approximately one-quarter of homogenate was separated for mRNA analyses, and the remaining portion was subsequently homogenized in solution of T-PER (Pierce) and phosphatase and protease inhibitor mixtures (Thermo Scientific and Roche) and processed as previously described (60).

Flow Cytometry. Lymphocytes isolated from the spleen were immunophenotyped with fluorescent antibodies for the following cell surface markers for pan T cells: PE-conjugated CD3e (500A2; BD Biosciences), PerCP-eFluor710–conjugated CD3e (17A2; eBioscience); CD4 and CD8 T cells: PE-conjugated CD4 (GK1.5; BD Biosciences), Pacific Blue-conjugated CD4 (RM4-5; Biolegend), APC-conjugated CD8 (Ly-2; BD Biosciences), PE/Cy7-conjugated CD8 (53-6.7; eBioscience); NK cells: APC-conjugated CD49b (DX5; BD Biosciences), PE-conjugated NK1.1 (PK136; Biolegend); B cells: FITC-conjugated CD45R/B220 (RA3-6B2; BD Biosciences), Alexa Fluor 710-conjugated CD19 (ebio1D3; eBioscience). All cells for flow cytometry were FC blocked with anti-CD16/32 (1:200; BD Biosciences) for 10 min at 4 °C before staining with surface marker antibodies. Cells were run on an LSRII flow cytometer (BD Biosciences) or BD FACSAria II (BD Biosciences) and analyzed with FlowJo software (FlowJo).

Immunoblotting. SDS/PAGE Western blot and dot blot were performed according to previously established protocols (60). Primary antibodies used for Western blot analysis included the following: 6E10 (BioLegend) and PS1 (Novus Biologicals). Following initial labeling, blot membranes were stripped in 0.2 M NaOH for 20 min followed by block and labeling with anti-GAPDH (Santa Cruz) as loading control.

Intracranial Injection of IgG. Direct injection of IgG into hippocampus was adapted from previous published reports (38). Stereotaxic injection of whole-molecule IgG (Jackson ImmunoResearch) was performed according to previously described surgical protocols (38, 60). Briefly, 4-mo-old mice were anesthetized and placed in stereotaxic frame (Kopf) under continuous isoflurane anesthesia. Using 10-μL Hamilton syringe and 30-gauge needle, mice received 2-μL injection of 1 mg/mL IgG in the right hemisphere and 2 μL of 0.01 M PBS in the left hemisphere at the following coordinates relative to bregma: anteroposterior, −2.06 mm; dorsoventral, −2.25 mm; mediolateral, ±1.5 mm. Needle was cleaned with consecutive washes of PBS, 70% (vol/vol) ethanol, and PBS in between hemispheres and animals. Animals were allowed to recover on heating pad before being placed back in home cages. One week following surgery, animals were perfused with 0.01 M PBS and entire brain removed for immunohistochemistry, confocal microscopy, and IMARIS analysis as described above.

BBB Permeability Assay. Evans Blue dye injection and BBB permeability analysis were performed according to a previously published protocol (33). Mice were injected i.p. (4 mL/kg) with 2% (wt/vol) Evans Blue (Sigma-Aldrich) in PBS. After 6 h, mice were perfused, and liver, kidney, and brain were removed and placed on ice. Organs were homogenized in PBS at 150 mg/mL (vol/wt) and centrifuged at 10,000 × *g* for 10 min, and then supernatant was loaded onto a clear 96-well plate in duplicate. Intensity of Evans Blue dye was then measured by spectroscopy at 595 nm. An uninjected mouse acted as a blank control, and its tissue absorbance values were subtracted from experimental animal values.

Mouse IgG ELISA. Total mouse IgG levels were measured by ELISA according to manufacturer's protocol (eBioscience). Mouse brain homogenate was loaded neat and normalized to the total protein content of each sample. Mouse plasma samples were diluted 1:10,000 as directed by manufacturer before being loaded onto the plate.

Multiplex ELISA Assays. Quantitative biochemical analysis of mouse cytokine and human Aβ were conducted using commercially available electrochemiluminescent multiplex assay system [Meso Scale Discovery (MSD)]. Human Aβ triplex (6E10 capture antibody) was used for simultaneous measurement of Aβ38, Aβ40, and Aβ42 in both soluble and insoluble protein fractions. Mouse proinflammatory panel 1 was used for simultaneous measurement of proinflammatory cytokines in soluble brain protein fraction.

qPCR. cDNA was produced from sample mRNA using Applied Biosystems High Capacity RNA-to-cDNA Kit (Thermo Fisher Scientific). All samples were then run in triplicate per gene on 384 qPCR plates using Applied Biosystems Gene Expression Master Mix (Thermo Fisher Scientific) according to manufacturer's protocol using the following TaqMan primers: Human *APP* (Hs00169098_m1), Human *PSEN1* (Hs00997789_m1), *Adam10* (Mm00545742_m1), *Adam17* (Mm00456428_m1), *Bace1* (Mm00478664_m1), and *Bace2* (Mm00517138_m1). Both probe only and probe plus RNA were run in triplicate per gene as negative controls. Plates were run immediately after loading on a Viia 7 Real-Time PCR System (Thermo Fisher Scientific). CT values were exported to Microsoft Excel and ΔΔct values and fold overexpression were calculated. Results are reported as fold overexpression relative to WT-5xfAD animals ± SEM.

BV-2 Microglial Cell Line Culture. The BV2 immortalized microglial cell line (63) [generously provided by Dr. Andrea Tenner (University of California, Irvine)] was cultured in complete media and incubated at 37 °C with 5% CO_2. Complete media was composed of DMEM high glucose (25 mM) supplemented with 10% (vol/vol) heat-inactivated FBS, sodium pyruvate (1 mM), Glutamax dipeptide (2 mM), and 1% penicillin/streptomycin.

Fibrillar Aβ Preparation. Fibrillar fluorescent Aβ ($fA\beta_{1-42}$) was generated as described previously (36). Briefly, fluorescently labeled $A\beta_{1-42}$ peptide (Anaspec) was first dissolved in 0.1% NH_4OH to 1 mg·mL^{-1}, and then further diluted in sterile endotoxin-free water and incubated for 7 d at 37 °C. fAβ was thoroughly mixed before cell exposure.

Analysis of Phagocytosis Signaling Pathways. BV2 microglial cells were cultured as described (see *BV-2 Microglial Cell Line Culture*). Twenty-four hours before phagocytosis assay, cells were passaged and plated on chamber slides (Thermo Fisher Scientific)

at density of 25,000 cells per chamber. Twelve hours before assay, cells were switched to serum-free media mirroring previous phagocytosis experiment. Thirty minutes before experiment, cells were treated with vehicle (DMSO), PI3K inhibitor, 20 nM wortmannin (Cell Signaling), or 50 μM Src/Syk kinase inhibitor, 3,4-methylenedioxy-β-nitrostyrene (MNS) (Tocris Bioscience). Following pretreatment, PBS or IgG (0.5 mg/mL) in addition to Aβ (5μg/mL) were added to the wells. After 30 min, cells were washed four times in prewarmed PBS and placed in 4% PFA for 30 min, followed by two subsequent PBS washes. Bright-field phase and fluorescent images were taken using Olympus IX71 microscope and 4× objective. Pictures from three independent wells per treatment were used for analysis by blind observer. Optical density of fluorescent images was measured following background subtraction using ImageJ and total cells per field were counted using the bright-field image and manual cell counter plugin of ImageJ.

Statistical Analysis. Statistical analysis was performed using Statview 5 statistics and GraphPad Prism 6 software. Comparisons involving more than two groups used one-way ANOVA followed by Fisher's post hoc test. Comparisons of two groups used two-tailed Student's *t* test. All differences were considered significantly different when $P < 0.05$.

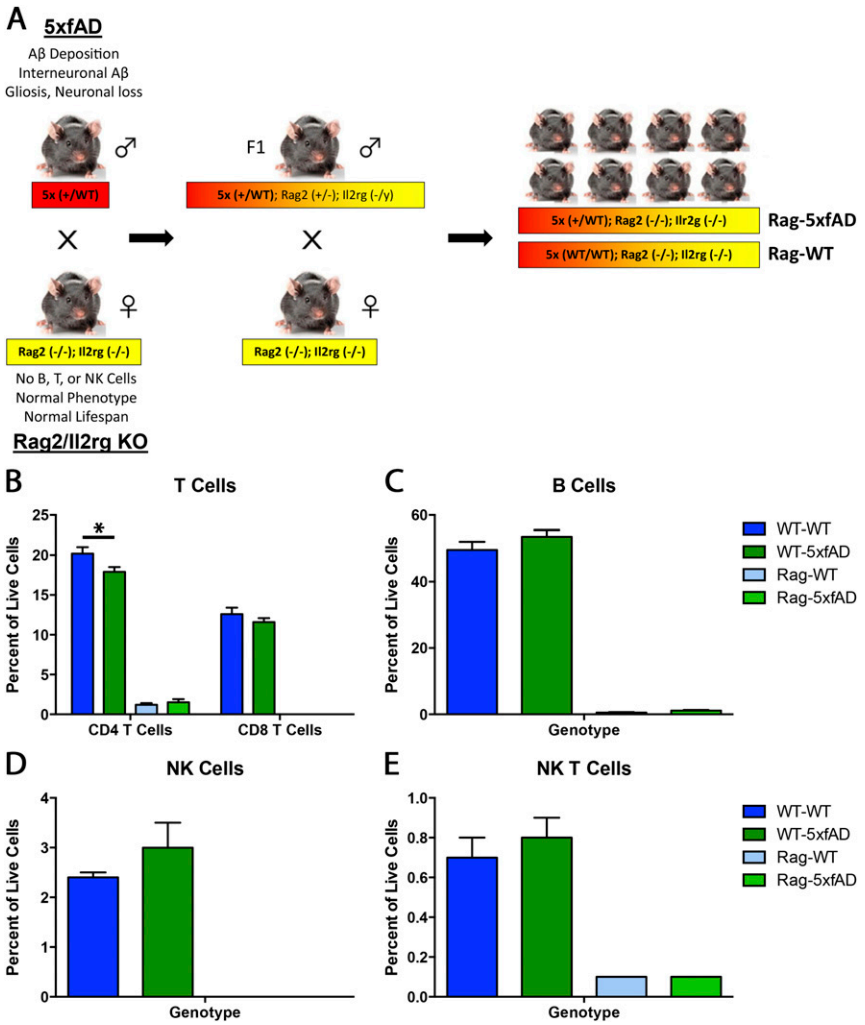

Fig. S1. Breeding paradigm and immune phenotype confirmation of the Rag-5xfAD mouse model. (*A*) Abbreviated breeding diagram showing the strategy used to generate the Rag-5xfAD mouse model and controls. (*B–E*) Flow cytometry performed on splenocytes of 6-mo-old animals confirmed that all immune-incompetent animals lacked B, T, and NK cells regardless of AD transgene status. Analysis of immune-competent animals revealed that percentages of these cell populations were not significantly different between WT-WT and WT-5xfAD animals except in the case of CD4 T cells (*B*), which were significantly decreased in WT-5xfAD mice vs. WT-WT mice. $n \geq 6$ animals/group and $^*P < 0.05$.

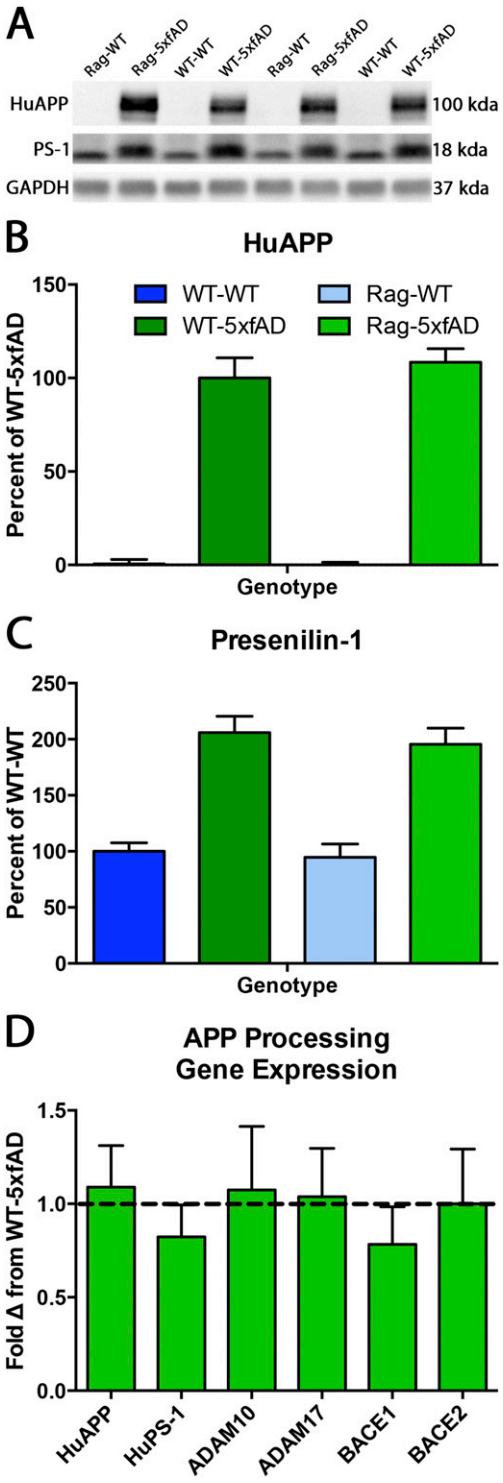

Fig. S2. Increased amyloid burden is not the result of increased APP expression or processing. (*A*) Western blot images of APP, PS-1, and GAPDH. (*B* and *C*) Quantification of Western blots demonstrates that neither APP nor PS-1 protein levels are significantly changed between WT-5xfAD and Rag-5xfAD animals. (*D*) Fold change in gene expression from qPCR further demonstrates no change in *APP* or *PSEN1* as well as key APP-processing enzymes: *Adam10*, *Adam17*, *Bace1*, and *Bace2*.

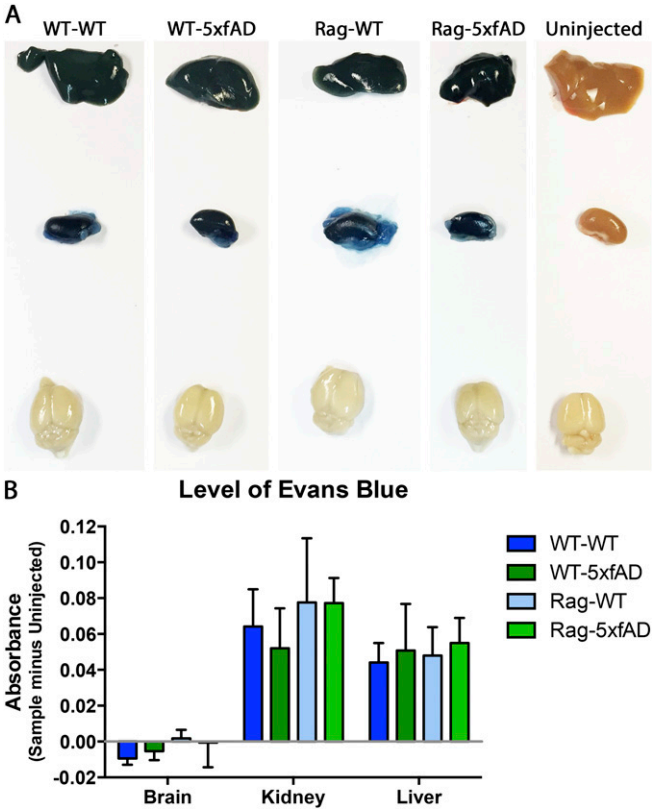

Fig. S3. Evans Blue analysis demonstrates no detectable changes in general BBB permeability. (*A*) Representative pictures of the liver, kidney, and brain of WT-WT, WT-5xfAD, Rag-WT, Rag-5xfAD, and uninjected control mice after killing and perfusion. (*B*) Spectroscopy analysis for levels of Evans Blue was used to measure changes in permeability according to previously published protocols (33). Analysis revealed no detectable levels of Evans Blue in the brains of any of the four genotypes and significant levels in both peripheral tissues examined. Absorbance values of uninjected control tissue was subtracted from the recorded absorbance of all tissue from all four genotypes. Data represented as mean ± SEM; $n = 3$ animals/genotype.

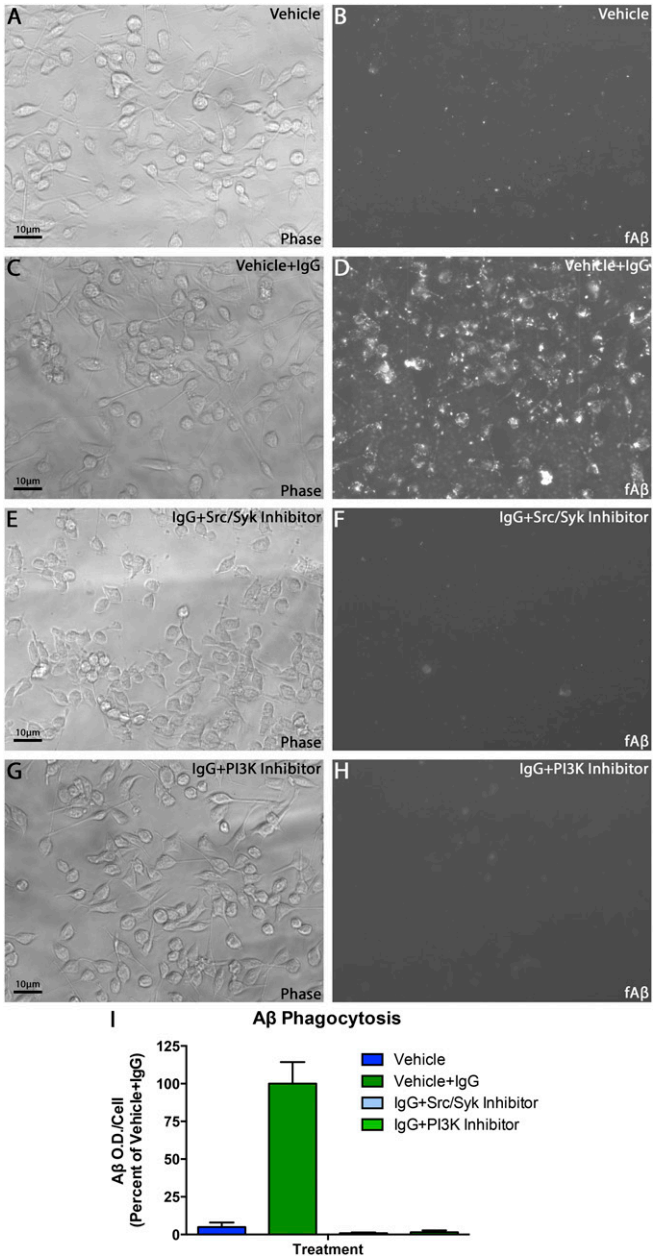

Fig. S4. Preimmune IgG is sufficient to induce robust Aβ phagocytosis. (*A*–*H*) Representative bright-field and fluorescent images of fibrillar Aβ phagocytosis within BV2 microglial cells after treatment with IgG and inhibitory drugs. (*A* and *B*) Microglial cells exhibited low levels of phagocytosis when treated with vehicle alone compared with treatment with vehicle plus IgG (*C* and *D*). Pretreatment with Src/Syk inhibitor (MNS; 20 μM) (*E* and *F*) or PI3K inhibitor (wortmannin; 50 nM) (*G* and *H*) completely eliminated the induction of phagocytosis by IgG. (*I*) Quantification of fluorescent Aβ optical density divided by cell count from bright-field images further illustrates elimination of phagocytosis. Vehicle-plus-IgG phagocytosis levels were significantly different from all other groups: ANOVA, $P < 0.0001$. Data are represented as mean ± SEM. ANOVA, $P < 0.05$, and Fisher's PLSD post hoc; $n = 3$ wells/group.

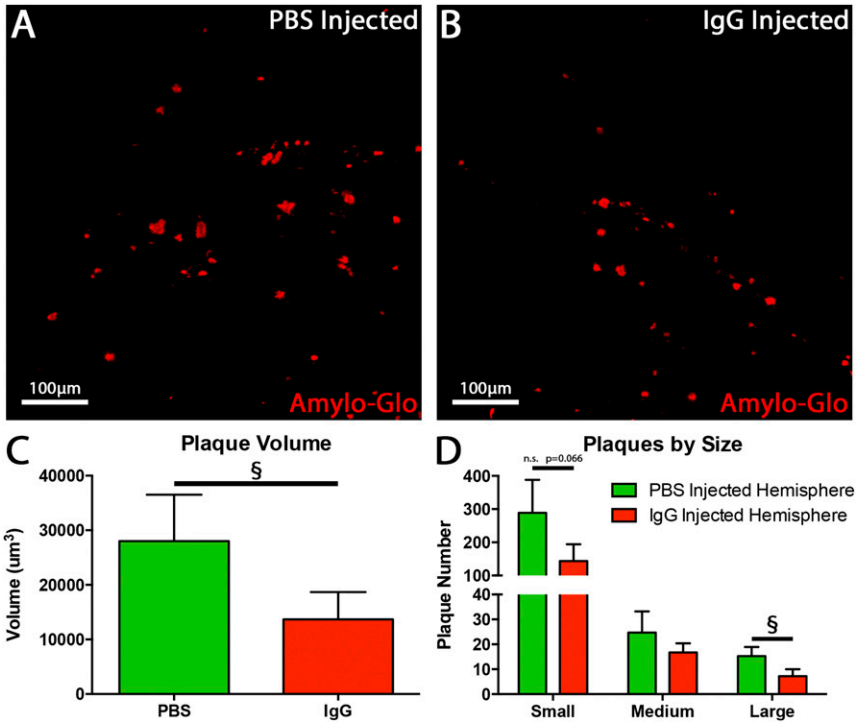

Fig. S5. Direct intrahippocampal injection of IgG reduces Rag-5xfAD plaque load in vivo. (*A* and *B*) Representative immunohistochemical images demonstrate significantly more amyloid present in the PBS-injected side (*A*) compared with the IgG-injected side (*B*). (*C* and *D*) IMARIS-based 3D quantification of Aβ confirms a significant reduction in both total Aβ volume and the number of large plaques, whereas the number of small plaques was almost significantly reduced ($P = 0.066$) as well. Data are represented as mean ± SEM; $n = 3$ animals/genotype. Student's *t* test (paired, two-tailed), $^{\S}P < 0.01$.

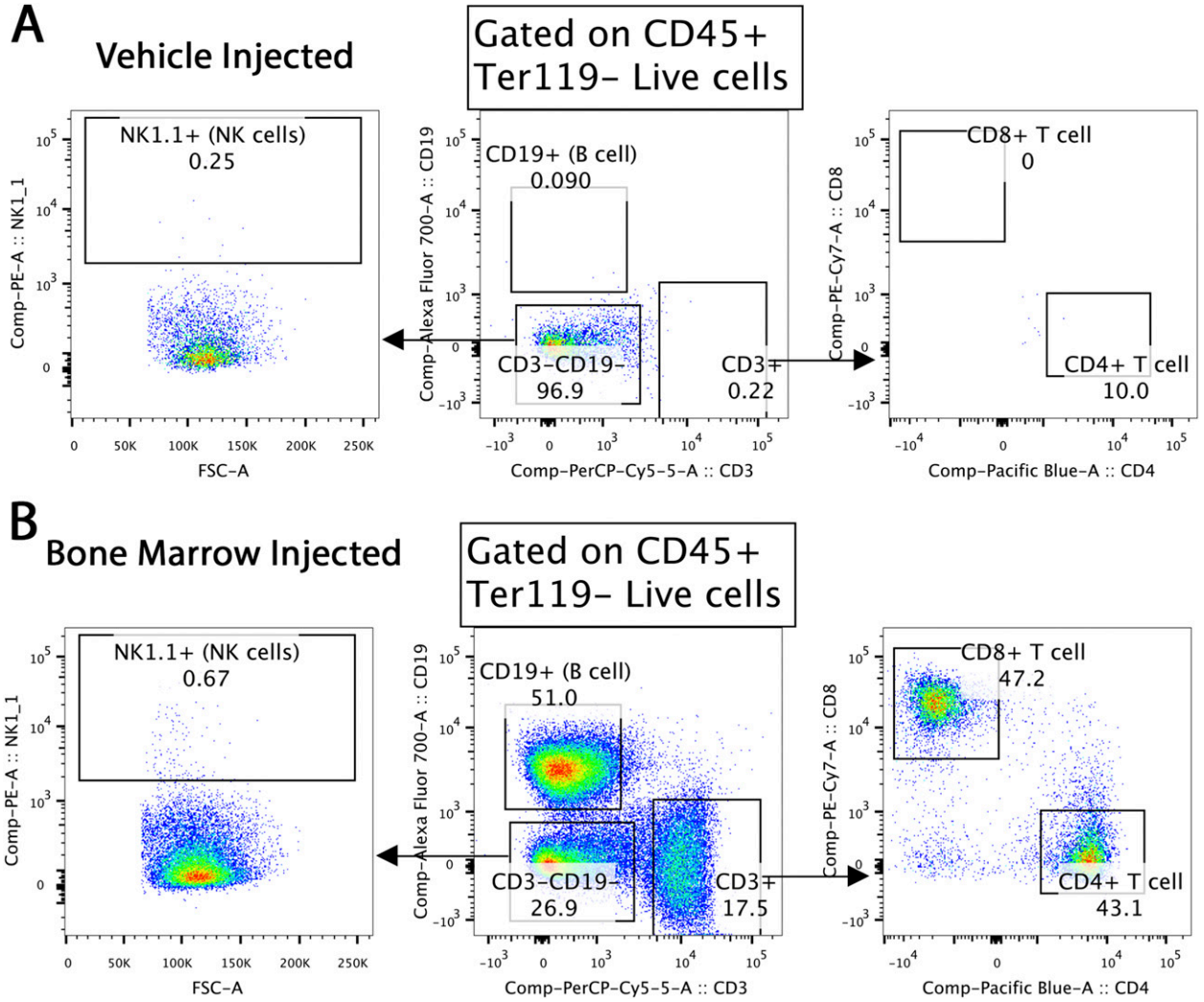

Fig. S6. Transplanted bone marrow survives and engrafts long-term in Rag-5xfAD mice. (*A* and *B*) Representative flow cytometry analyses of tissue from Rag-5xfAD vehicle- and bone marrow-treated animals at time of killing (4 mo posttransplant). (*A*) Rag-5xfAD mice receiving vehicle were predictably immune-incompetent lacking true positive labeling for B, T, or NK cells. (*B*) Rag-5xfAD mice receiving bone marrow demonstrate robust engraftment of both B and T cells, and to a lesser extent NK cells, 4 mo posttransplantation.

Other Supporting Information Files

Dataset S1 (XLSX)